©2004 by Economic Geology
Vol. 99, pp. 691–712

The Gandy and Abolhassani Epithermal Prospects in the Alborz Magmatic Arc, Semnan Province, Northern Iran

Gholam Hossein Shamanian,[†,*]

Department of Geology, University of Shahid Beheshti, Tehran, Iran

Jeffrey W. Hedenquist, Kéiko H. Hattori,

Department of Earth Science, University of Ottawa, Ottawa, Ontario K1N 6N5, Canada

and Jamshid Hassanzadeh

Department of Geology, University of Tehran, Tehran, Iran

Abstract

The Gandy and Abolhassani epithermal precious and base metal deposits occur in the Torud-Chah Shirin mountain range in the Alborz magmatic belt of northern Iran. The mountain range is considered to be part of the Paleogene Alborz volcanic arc. The exposed rocks in the study area consist of a volcaniclastic sequence of thin-bedded siltstones and sandstones, lapilli tuffs, volcanic breccias, and intermediate lava flows at Gandy, and mostly andesitic flows at Abolhassani. The flows are middle to upper middle Eocene age and they show a typical arc geochemical signature, with low concentrations of Nb, Ta, Zr, Hf, and Ti.

Variable hydrothermal alteration occurs in scattered outcrops, covering about 4 km^2 at Gandy and 1 km^2 at Abolhassani. The Gandy and Abolhassani areas are about 3 km apart, and each contains a small abandoned Pb-Zn mine. Mineralization at Gandy occurs in quartz sulfide veins and breccias and is accompanied by alteration halos of quartz, illite, and calcite up to 2 m wide. The mineralization is divided into three main stages: brecciation (I), fracture filling (II), and crustiform banding (III). Stage I is economically important in terms of precious metal content. Stage II consists of four substages and contains the majority of base metal ore with quartz, calcite, and barite. Native gold is commonly found within partially oxidized pyrite and secondary iron (hydr)oxides such as goethite in stage I and coexists with galena and chalcopyrite in stage II. The final stage is dominated by quartz and calcite. Mineralization in the Abolhassani veins occurred in three main stages. The first two stages, which are economically important, contain similar mineral assemblages, including quartz, calcite, barite, galena, sphalerite, pyrite, and chalcopyrite, whereas the final stage is dominated by quartz and calcite. No gold grains were found in the Abolhassani samples. The average (max) assays from 14 channel samples of Gandy veins are 14.5 (68.3) g/t Au, 30.6 (161) g/t Ag, 3.1 (13) wt percent Pb, 0.84 (3.8) wt percent Zn, and 1.0 (6.3) wt percent Cu. For comparison, the values from 19 channel samples of Abolhassani veins are 0.85 (6.0) g/t Au, 29.5 (115) g/t Ag, 6.4 (16.5) wt percent Pb, 1.2 (5.2) wt percent Zn, and 0.83 (7.7) wt percent Cu.

Fluid inclusion and sulfur isotope compositions were analyzed for the sulfide-sulfate assemblages of stage II at Gandy and stages I and II at Abolhassani. In both cases fluid inclusion assemblages were examined mostly in subhedral crystals of sphalerite. The average homogenization temperatures (T_h) and salinities of fluid inclusion assemblages from Gandy range from 234° to 285°C, with a peak at about 250°C and 4.2 to 5.4 wt percent NaCl equiv. These T_h values are in good agreement with isotopic temperatures from two sphalerite and galena pairs (236° and 245°C). The temperature and salinity values in fluid inclusion assemblages from the Abolhassani deposit range from 234° to 340°C and 6.7 to 18.7 wt percent NaCl equiv. Sulfide pairs of sphalerite-galena do not give reasonable isotopic equibrium temperatures at Abolhassani. Comparison of T_h versus ice melting ($T_{m(ice)}$) values for the two deposits indicates the presence of a moderate-salinity fluid (5–6 wt % NaCl equiv) of similar temperature (~250°C) in each deposit but with a higher temperature and salinity component also present at Abolhassani. The base metal-rich mineralization at Abolhassani may thus have been caused by the periodic injection of this higher salinity fluid. The Abolhassani deposit has a higher average Ag/Au ratio (~35) and Pb + Zn concentration (up to 7.6 wt %) than Gandy (Ag/Au ~ 2 and 3.9 wt %), consistent with this interpretation.

The minimum depth of formation was at least 430 m below the paleowater table for Gandy and possibly as much as 600 m at Abolhassani. The lower grades of gold and the presence of higher salinity fluids at Abolhassani suggest that the occurrence of higher grade precious metal zones is unlikely at greater depth. By contrast, Gandy may have potential at depth for extensions of the high-grade gold veins. Exploration in the region should focus on areas with geologic evidence for relatively little posthydrothermal erosion, <200 to 300 m, thus increasing the preservation potential of epithermal veins with high gold grades, similar to those at Gandy. Results from Gandy and Abolhassani may aid exploration and assessment of the numerous, untested epithermal and related prospects along this 1,800-km-long volcanic belt in northern Iran.

[†] Corresponding author: email, shamanian@yahoo.com

[*] Present address: Department of Geology, Faculty of Science, Gorgan University of Agricultural Sciences and Natural Resources, Gorgan, Golsten Province, Iran.

0361-0128/01/3430/692-22 $6.00

Introduction

THE TORUD-CHAH SHIRIN mountain range of Semnan Province is located in the eastern part of the Alborz mountain system, which crosses northern Iran for about 1,800 km from the border with Afghanistan in the east to the Caucasus border in the northwest (Fig. 1). A regional stream-sediment geochemical survey in the first half of the 1990s by the Geological Survey of Iran located a number of precious metal anomalies that have subsequently been traced to sources from epithermal prospects. This paper describes the epithermal occurrences of this region and focuses on two such prospects, Gandy and Abolhassani, in the Moaleman area, ~300 km east of Tehran. The Gandy and Abolhassani areas, located at 35° 20' N and 54° 38' E, are characterized by high precious and base metal anomalies, respectively. This paper compares these two prospects and discusses their relative depths of erosion and the significance for exploration in the region.

The Gandy and Abolhassani areas are about 3 km apart (Fig. 1) and each contains a small abandoned Pb-Zn mine. They were in operation from 1960 to 1970. There are many other showings and abandoned mines of mostly base metal veins in the Torud-Chah Shirin range. The regional geochemical exploration project from 1990 to 1996 covered 42,000 km^2 in north-central Iran, producing 26 map sheets at a scale of 1:100,000, including the Torud-Chah Shirin range (Geological Survey of Iran, 1995). Based on the survey results, five districts were considered prospective, including Gandy and Abolhassani, and were recommended for detailed prospecting for Au, Cu, Pb, and Zn.

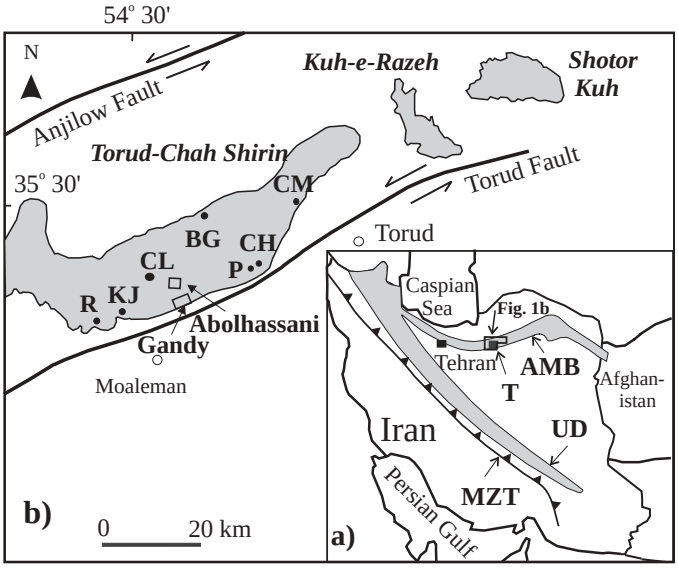

FIG. 1. Location of two main Tertiary volcanic belts in Iran: the NW-trending Urumieh-Dokhtar (UD) zone, which runs parallel to the main Zagros thrust (MZT) cutting central Iran, and the Alborz magmatic belt (AMB) in northern Iran. The Central Iranian Eocene volcanic zone, also called Lut volcanic rocks, is located between the AMB and the MZT in eastern Iran and not shown in the diagram. The exposed rock units of the Torud (T) area include the Paleozoic Shotor-Kuh range, the Mesozoic Kuh-e-Reza range, and the Paleogene Torud-Chah Shirin range. A variety of epithermal and other deposit types occur in the Torud-Chah Shirin mountain range in addition to those in the Gandy and Abolhassani prospects. District names: BG = Baghu, CH = Cheshmeh Hafez, CL = Chalul, CM = Chahmessi, KJ = Khanjar, P = Pousideh, R = Reshm. Modified from Hushmandzadeh et al. (1978).

Field observations and data collected prior to this study (Geological Survey of Iran, 1995; Kousari, 2001) suggested that these two areas host precious as well as base metal mineralization of epithermal character. These include: (1) typical host rocks (volcanic, volcaniclastic, and sedimentary rocks); (2) deposit form (vein and breccia); (3) vein textures such as fine and coarse bands, crustiform bands, and hydrothermal breccias; (4) gangue minerals such as quartz, carbonate, and barite; (5) sulfides such as galena, sphalerite, chalcopyrite, pyrite; and (6) enrichment of Au, Ag, As, Sb, Hg, Pb, and Zn.

Earlier work in the area (Geological Survey of Iran, 1995) focused on the regional geology and geochemical exploration. The present study includes mapping of host rocks, alteration, and veins at a scale of 1:50,000, examination of the composition of ore minerals and the alteration assemblages, microthermometry of fluid inclusion assemblages, and sulfur isotope analysis of sulfide and sulfate minerals. These data help constrain the ore-forming environment and the depth of erosion of the exposed veins, the latter a critical feature in determining the depth potential of these prospects.

Regional Setting

The Torud-Chah Shiran range lies in the central to eastern portion of the Alborz mountain system, a mountain chain of complex tectonic, magmatic, and stratigraphic history (summarized by Alavi, 1996). On the basis of regional tectonic considerations, Alavi (1991, 1996) suggested that the Torud-Chah Shiran range and volcanic rocks in the adjacent areas are related to Eocene magmatism in the Central Iran magmatic zone to the south and not to the volcanic rocks of the Alborz magmatic belt to the west. The distribution of Tertiary igneous rocks shows that the western portion of the Alborz arc merges with another Tertiary calc-alkaline magmatic belt, the Urumieh-Dokhtar zone, which runs parallel to the main northwest-trending Zagros thrust (Fig. 1). Recently, Hassanzadeh et al. (2002) suggested that the two belts were once a single arc but separated by intra-arc extension that started in the late Eocene. Based on the latter view, the Alborz magmatic belt includes Torud-Chah Shiran and represents the northern half of the proto-arc. This arc is characterized by thick accumulations of early to middle Eocene submarine green tuffs (equivalent to the Karaj Formation of central and western Alborz), followed by late Eocene, to possibly early Oligocene, submarine to subaerial lava flows which locally include nepheline-normative and shoshonitic rocks. A series of silica-saturated volcanic rocks occur locally. The intra-arc spreading formed sedimentary basins between the Alborz range and Central Iran, an area characterized by Oligocene mafic-alkaline magmatism (Hassanzadeh et al., 2002). Chemical compositions of volcanic rocks presented below indicate that Torud-Chah Shiran rocks have a typical arc signature, consistent with this proposed interpretation.

The Torud-Chah Shirin range consists mainly of igneous rocks of Tertiary age, although there are also scattered outcrops of metamorphosed Paleozoic and Mesozoic rocks. Peak magmatic activity occurred from middle to possibly late Eocene and has been divided into three stages, from oldest to youngest (Fig. 2; Hushmandzadeh et al., 1978) as

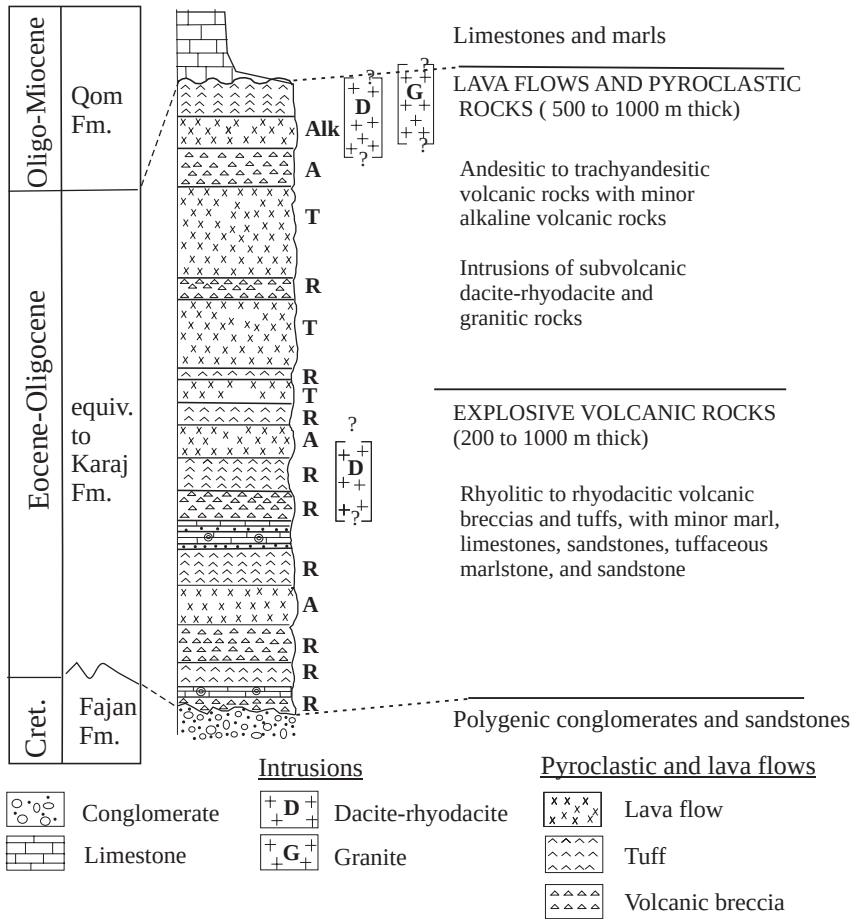

FIG. 2. Tertiary magmatic events in Torud-Chah Shirin mountain range (modified from Hushmandzadeh et al., 1978). A = andesitic, R = rhyolitic to rhyodacitic compositions, T = trachyandesitic.

follows: (1) explosive volcanic activity represented by rhyolitic to rhyodacitic tuffs and locally andesitic lava flows, with subordinate marls, tuffaceous marlstones, and sandstones; (2) lava flows and pyroclastic rocks of andesite, trachyandesite, and basaltic andesite composition; and (3) subordinate dacitic-rhyodacitic rocks and hypabyssal intrusive rocks. Structural patterns are controlled by two principal strike-slip faults, Anjilow in the north and Torud in the south, both with northeast trends (Fig. 1).

Similar to the rest of the Alborz, the Paleogene igneous rocks of Gandy and Abolhassani are mostly shoshonitic or high K calc-alkalic in composition. The chemical compositions of five volcanic rock samples from this area (Table 1, Appendix 1) include the first documentation of minor and trace elements from volcanic rocks of the Torud-Chah Shirin range. They are characterized by high concentrations of large ion lithophile elements and low concentrations of high field strength elements (Fig. 3), typical of arc igneous rocks (e.g., Pearce and Peate, 1995). These data are consistent with the conclusions from other studies on the tectonic setting of the Paleogene rocks of the Alborz magmatic belt (e.g., Alavi, 1996; Hassanzadeh et al., 2002).

The Torud-Chah Shirin mountain range hosts many mineral showings and abandoned mines (Fig. 1), particularly epithermal base metal veins. In addition to Gandy (Au-Ag-Pb-Zn) and Abolhassani (Pb-Zn-Ag-Au), other occurrences include Cheshmeh Hafez (Pb-Zn), Chalu (Cu), Chahmessi (Cu), and Pousideh (Cu). Other types of deposits in this range include placer gold, an underground mine for turquoise at Baghu, skarn deposits, and Pb-Zn deposits in carbonate rocks. The Baghu gold placer is located ~15 km north of the study area, and the gold is probably the product of weathering of nearby quartz sulfide veins hosted by andesitic volcanic rocks. The presence of tourmaline in the wall rocks of these veins may indicate proximity to a porphyry system. An abandoned iron skarn deposit is located at the contact of Cretaceous limestones, andesitic lava flows, and a quartz monzonite stock ~2 km northwest of the study area. Reshm and Khanjar are abandoned Pb-Zn mines located ~15 and ~10 km, respectively, west of the study area. Ore in these localities occurred principally as veins in Cretaceous dolomitic limestones and consisted of quartz, calcite, galena, sphalerite, and pyrite.

Paleogene volcanic rocks also occur in other parts of the eastern Alborz arc. High K calc-alkalic and feldspathoid-bearing rocks are common to all series in this general area (e.g., Spies et al., 1983; Khalatbari, 2000). Taheri and Shamanian (2001) mapped the north Kashmar area, ~400 km east of Gandy and Abolhassani, and reported a similar volcanic

series. Geochemical prospecting by the Geological Survey of Iran has led to discoveries of anomalies and ore occurrences associated with these rocks, including the Arghash deposit (Au-Sb), located ~50 km south of Nishabour. The mineralization at Arghash occurs in veins which consist of microcrystalline quartz with calcite, stibnite, pyrite, and chalcopyrite (Shamanian, 1998). The grade in the quartz-calcite veins ranges up to 7 g/t Au. The presence of microcrystalline quartz and stibnite, and the low content of base metals in the veins, suggest that there may have been relatively little erosion of this epithermal prospect.

TABLE 1. Composition of Volcanic Rocks in the Gandy and Abolhassani Areas

Sample no.	79/H78 Rhyolitic tuff	TR52-7 Andesite	79/H40 Andesite	TA1/6 Basaltic andesite	79/A37 Andesite
SiO_2 (wt %)	67.7	51.6	56.9	47.5	54.3
TiO_2	0.6	1.1	0.7	0.9	0.6
Al_2O_3	12.6	16.6	16.5	14.5	13.7
Fe_2O_3	1.2	7.9	3.1	8.3	5.7
MnO	0.1	0.3	0.1	0.2	0.1
MgO	0.2	1.3	0.3	7.6	1.1
CaO	4.3	4.5	6.4	8.3	8.1
Na_2O	<0.005	0.4	1.0	1.9	2.4
K_2O	4.7	5.8	4.0	1.9	3.4
P_2O_5	0.2	0.6	0.2	0.3	0.3
L.O.I	6.5	8.5	9.0	7.3	8.8
Total	98.1	98.6	98.2	98.6	98.5
V (ppm)	52	190	160	210	160
Cr	79	140	31	360	76
Co	1.5	18.2	3.1	34.4	13
Ni	8.3	50	16	16	17
Zn	29	136	14	150	42
Rb	130	140	94	210	110
Sr	150	150	180	590	190
Y	127	18	18	17	12
Zr	31	80	110	88	53
Nb	4.7	18	9.6	7.0	6.0
Ba	1,000	950	670	330	790
La	26	31	28	16	22
Ce	56	67	58	35	46
Nd	25	31	26	19	24
Pb	45	110	16	51	10
Th	3.8	3.6	8.0	2.2	6.2
U	1.4	1.4	2.3	0.9	1.7
Ga	9.8	19	17	16	16
Cu	87	200	9.7	92	0.1
Mo	1.7	2.0	1.1	1.3	0.7
Ag	230	79	98	86	36
As	39	32	10	1.8	4.1
Cd	0.1	0.3	<0.01	0.1	0.1
Sb	6.4	8.8	1.9	3.0	1.1
Bi	0.2	0.3	0.2	0.2	0.3
W	1.3	1.5	1.5	0.4	0.5
Sn	1.0	1.7	1.8	1.0	1.4
Sc	4.1	13	12	19	14
Pr	7.0	8.6	7.3	4.9	6.1
Sm	4.7	6.0	5.5	4.3	4.9
Eu	1.0	1.2	1.2	1.1	1.0
Gd	3.5	5.5	4.6	4.1	3.9
Tb	0.4	0.6	0.6	0.5	0.4
Dy	2.6	4.1	3.6	3.7	2.6
Ho	0.4	0.6	0.6	0.6	0.4
Er	1.0	1.9	1.6	1.7	1.0
Tm	0.1	0.2	0.2	0.2	0.1
Yb	1.4	2.4	2.2	2.1	1.4
Lu	0.1	0.2	0.2	0.2	0.1
Hf	1.0	2.2	3.3	2.6	1.6
Li	55	27	89	55	12
Ta	0.3	1.0	0.7	0.4	0.4
Cs	0.9	2.2	6.3	0.9	5.5

Notes: Major elements, Cr, and Zn determined by XRF; total Fe expressed as Fe_2O_3; other elements determined by ICP-MS after digestion with HF-$HClO_4$-HNO_3; analyses at the Ottawa-Carleton Geoscience Centre

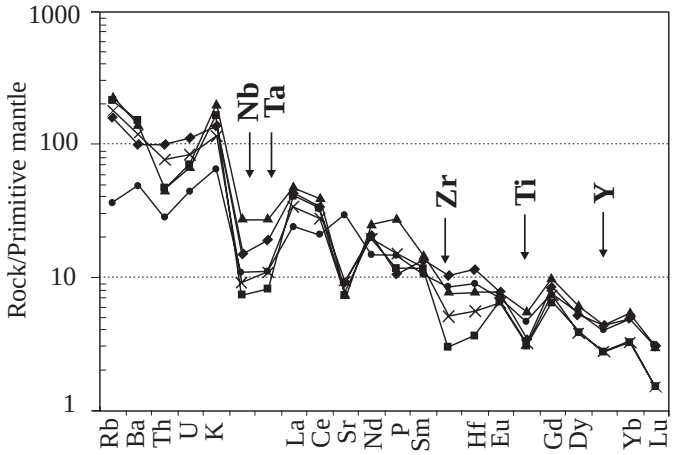

FIG. 3. Primitive mantle-normalized spidergrams for volcanic rocks from the Gandy and Abolhassani prospects (normalization after McDonough and Sun, 1995). The patterns with apparent lows at Nb, Ta, Zr, Hf, and Ti are typical of subduction zone arc magmas.

Local Geology

Gandy area

An area of about 8 km^2 was mapped at Gandy. Outcrops consist mainly of felsic pyroclastic rocks, intermediate lava flows and volcanic breccias, and epizonal felsic intrusions (Fig. 4). The local stratigraphy, from oldest to youngest, comprises the following:

1. A sequence of thin-bedded volcaniclastic siltstones and sandstones, with subordinate marlstones and tuffaceous sandstones in the lower part, forms the basal section (sample Ga-M-41, Appendix 1). Rhyolitic tuffs and tuffaceous sandstones with intercalated thin chert beds occur in the upper section (samples Ga-M-31 and 79/H78, Appendix 1), which is lower middle Eocene in age based on the fossil record (Hushmandzadeh, 1978). The thickness of individual tuff beds varies from 3 to 20 cm. In the Gandy area, this unit is about 250 m thick.

2. Lapilli tuffs, volcanic breccias, and intermediate lava flows (samples Ga-M-8, Ga-M-10, 79/H40, and TR-52-7, Appendix 1), of middle Eocene age based on fossil evidence, unconformably overlie the lower unit and are separated by a 20-m-thick basal conglomerate. This middle unit is about 200 m thick and is covered by a sequence of thin-bedded, coarse- to fine-grained sandstones and siltstones about 100 m thick (sample Zr-41, Appendix 1).

3. Rhyolitic to rhyodacitic domes (samples Ga-M-14 and 79/H12, Appendix 1) are the youngest rocks in the area. It is debatable whether they are Eocene or much younger in age.

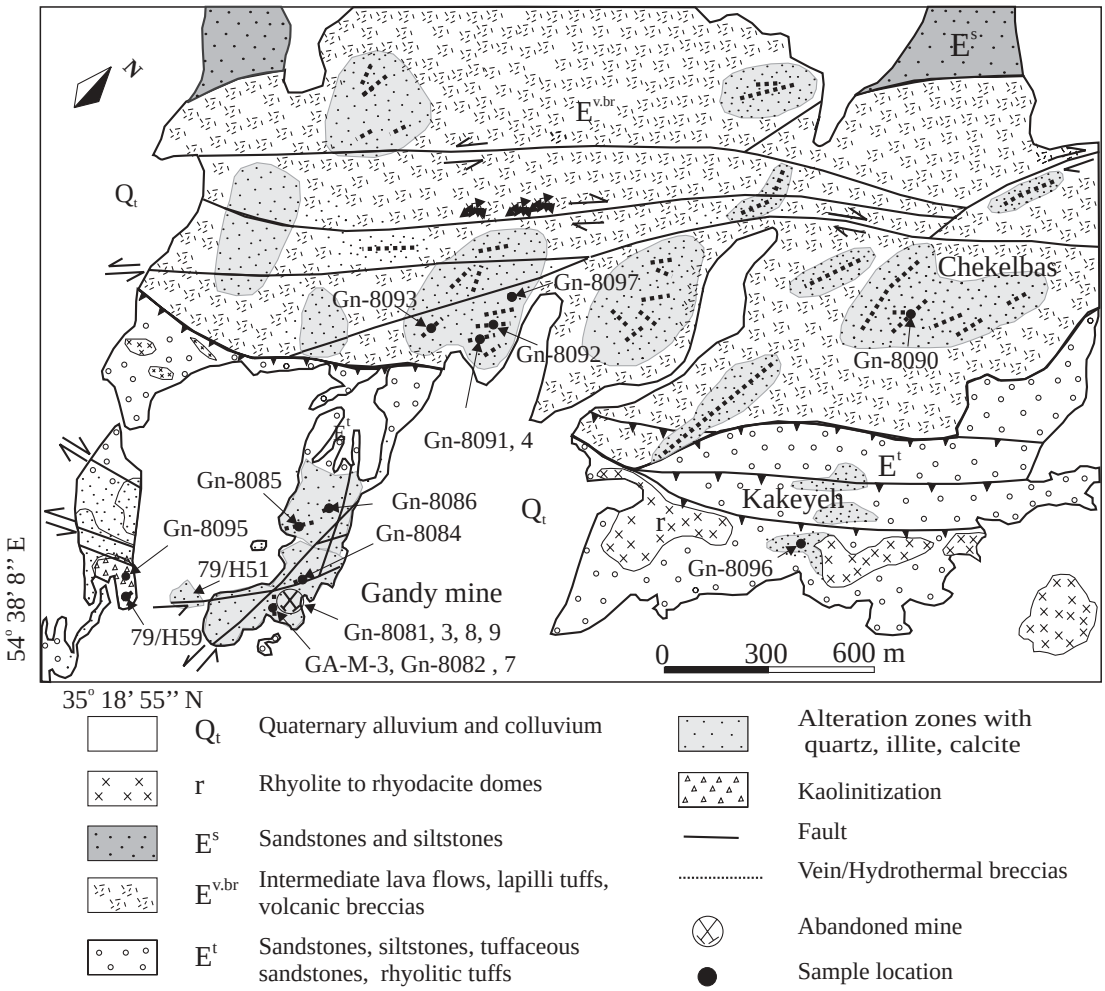

FIG. 4. Geologic map of the Gandy prospect. Latitude and longitude of the southwestern corner is shown.

The Torud fault is accompanied by minor faults and joints in the mapped area. The fractures and faults have N 50° to 60° E strikes (Fig. 4) and 50° to 80° SE dips and were formed by movement on the northeast-trending Torud fault.

Abolhassani area

Abolhassani is located ~3 km north of the Gandy area at an elevation of ~1,500 m, 200 m higher than Gandy. An area of about 4 km^2 was mapped. The outcrops consist mainly of andesitic volcanic rocks (Fig. 5). The local stratigraphy comprises the following:

1. A lower sequence of thin-bedded, coarse- to fine-grained sandstones, is middle to late Eocene in age based on fossil evidence (Hushmandzadeh, 1978).
2. Pyroclastic rocks and andesitic and trachyandesitic flows are also late Eocene in age, based on the fossils present in intercalated sedimentary rocks. Andesitic flows in the study area, which are about 400 m thick, belong to this unit (samples Zr-22, 79/A3, TA1/6, and 79/A37, Appendix 1) and were intruded by dacitic to rhyodacitic subvolcanic rocks (sample Zr-43, Appendix 1). This unit was also intruded by hypabyssal rocks such as a monzodiorite plug in the Abolhassani area (sample Zr-5, Appendix 1), a quartz monzonite stock 2 km northwest of Abolhassani (sample 79/A16, Appendix 1), and a granitic dike 1.5 km west of Abolhassani (sample 79/A13, Appendix 1). Their age is uncertain, possibly Oligocene or much younger.

Alteration and Vein Mineralogy

Veins and alteration halos

The area of about 1 km^2 centered on the old Gandy mine contains rocks that have been intensely altered. An additional area of about 4 km^2 contains scattered outcrops of altered rocks with intervening unaltered andesitic lava flows (Fig. 4). Mineralization occurs in veins and breccias, consisting mainly of carbonate minerals, quartz, barite, galena, sphalerite, pyrite, and chalcopyrite. The breccia zones are tabular in shape and strike N 50° to 70° E, and dip 60° SE to vertical. Their strike length ranges from 20 to 100 m and they vary in thickness, from 10 to 100 cm. The breccias include economically important gold and base metal sulfides in tabular, high-angle zones (<100 cm wide) in the old mine (Fig. 6A). The

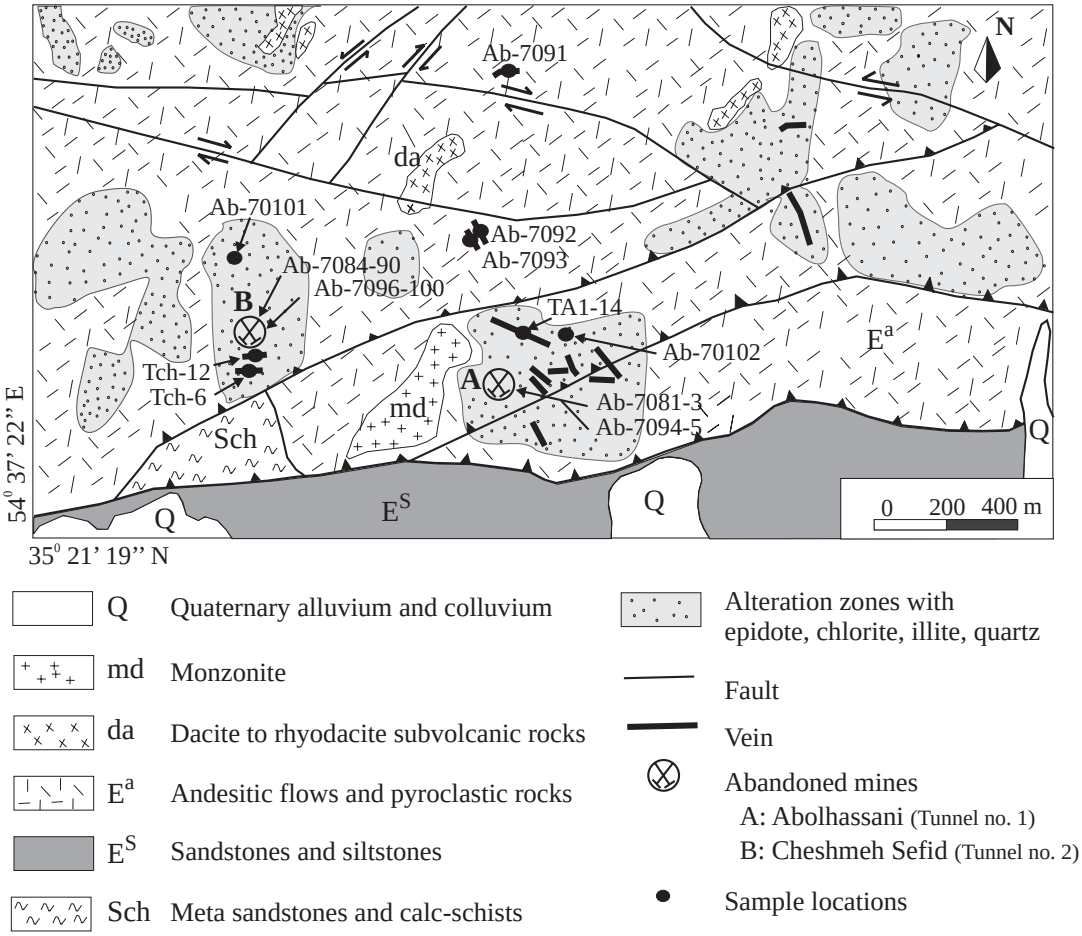

FIG. 5. Geologic map of the Abolhassani prospect. Latitude and longitude of the southwestern corner is shown.

veins include barren quartz-carbonate assemblages north of the Gandy mine and economically important but narrow veins (<30 cm) of base metal sulfides in the old mine.

The intense alteration in the central area occurs in rhyolitic tuffs and tuffaceous sandstones and is clearly associated with veins and veinlets as halos <2 m wide. The tuffs are strongly silicified. Illite is common and replaces feldspars and groundmass; chlorite is rare. Montmorillonite is uncommon but locally replaces feldspars. In the old Gandy mine, the ore-hosting tuffs are intensely altered to kaolinite. The kaolinite-rich horizons have been mined recently on a small scale for the ceramic industry. Rhyolitic tuffs are stained with secondary iron oxides such as limonite and goethite. Iron and manganese oxides as well as jarosite form boxworks after sulfides that coat the surfaces of fractures.

Exposures north of the Gandy mine are composed of unaltered to weakly altered intermediate lava flows. Intense alteration in this area, consisting of quartz, illite, and calcite, forms halos <1 m wide around quartz-calcite veins. Kaolinite forms a narrow 1- to 2-cm-wide band immediately adjacent to the veins and is probably related to oxidation of sulfides.

The abandoned mine at Abolhassani has two old tunnels named Abolhassani and Cheshmeh Sefid, which expose mineralized veins and breccias. The Abolhassani veins strike N50° to 60° W and dip 40° to 50° NE. Their strike length ranges from 20 to 50 m. The Cheshmeh Sefid veins strike N70° to 85° W and dip 40° to 50° NE, with lengths that range from 20 to 200 m. The veins and veinlets consist mainly of quartz with colloform textures, calcite, barite, and sulfides such as galena, sphalerite, pyrite, and chalcopyrite. Vein widths vary from 20 to 100 cm. Hydrothermal alteration is intense adjacent to veins and is up to 2 m wide, but variable intensity of alteration is exposed in scattered outcrops (Fig. 5). Epidote and chlorite are common and replace igneous biotite, hornblende, and pyroxene. Feldspars are partially altered to a mixture of illite and montmorillonite. Outside this area there are scattered patches of similar alteration along faults and joints.

Paragenetic sequence of mineralization at Gandy

Mineralization in the Gandy area can be divided into three main stages: brecciation (I), fracture filling (II), and crustiform banding (III). On the basis of crosscutting relationships, mineral assemblages, and textures, the main substages of mineralization are divided into several substages (Figs. 6–7).

Stage I: This stage is significant in terms of precious metal content, consisting of brecciated bodies with fragments of kaolinitized host rock up to 20 cm in diameter. The breccias

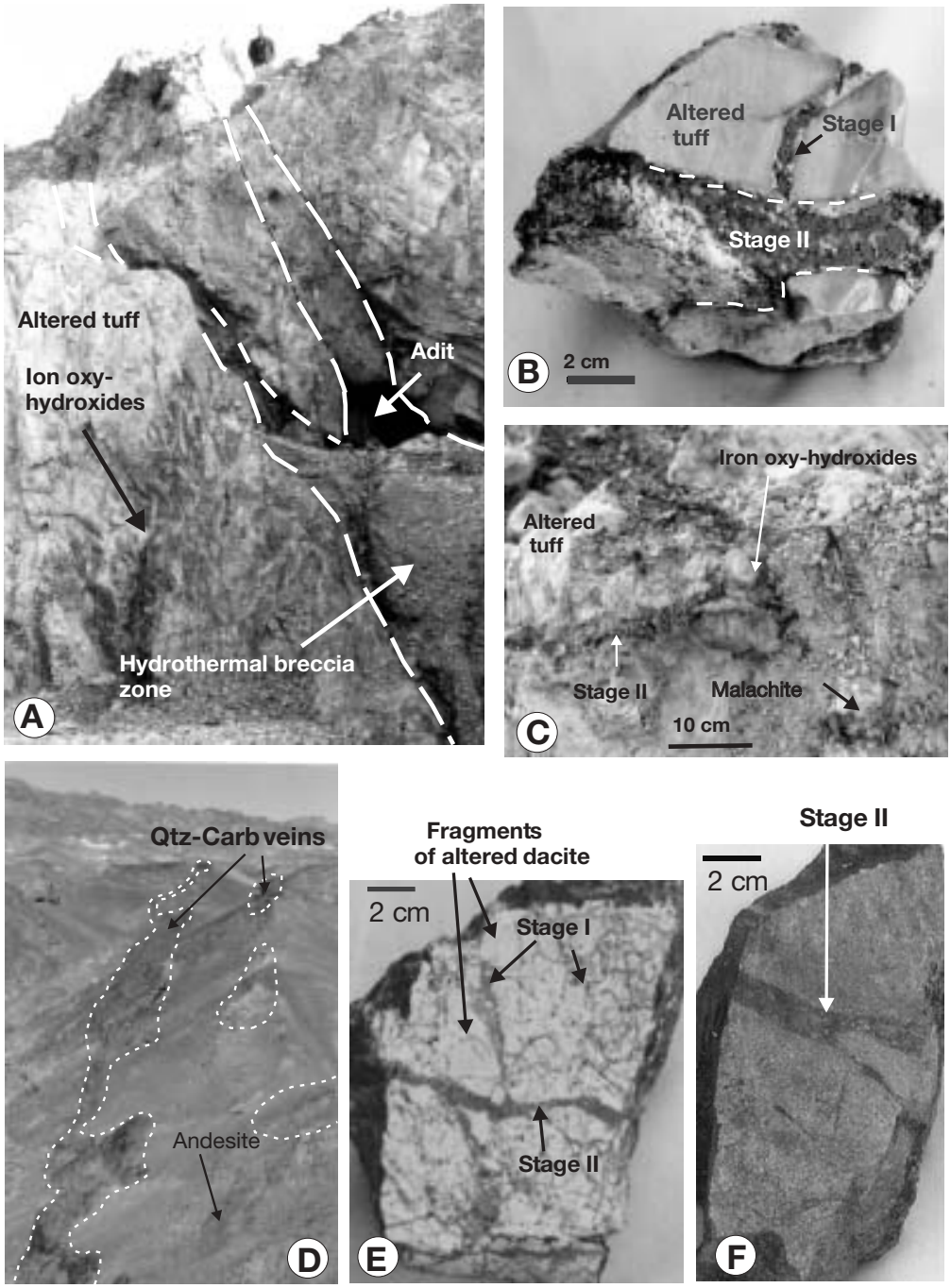

FIG. 6. Photographs showing three main stages of mineralization in the Gandy (A, B, C, and D) and Abolhassani (E and F) prospects: A. Hydrothermal brecciated zones of stage I with fragments of host tuff breccia that have been kaolinitized. The breccias are cemented by base metal sulfides, carbonates, and microcrystalline quartz. The host rock consists of thin- to medium-bedded tuffs with intercalated thin chert beds. Person standing on top for scale. B. Hydrothermal breccia of stage I, consisting of brecciated fragments of altered tuff that show a jigsaw-puzzle texture. The intensely kaolinitized fragments of host rocks are cemented by base metal sulfides plus microcrystalline quartz. The breccia was cut by a veinlet (5 cm wide) of base metal sulfides, barite, and microcrystalline quartz of the second stage of mineralization. C. Narrow veins of base metal sulfides, barite, and quartz of stage II. The host rock consists of thin-bedded rhyolitic tuffs with minor bedded chert (dark color) and is white due to intense kaolinitization. The weathering produced iron oxyhydroxides (yellow to brown), and malachite (green). D. Aerial view of stage III quartz-carbonate veins, looking north. Vein zones are outlined, with individual veins ranging from 20 to 100 cm in width, consisting of quartz, carbonate, pyrite, and chalcopyrite. Brown color of the veins is due to oxidation of pyrite. The host rock consists of altered andesite. Width of foreground ~15 m. E. Hydrothermal breccias of stage I mineralization in the Abolhassani prospect, consisting of brecciated fragments of altered dacite, up to 3 cm in diameter. The breccia was cut by a veinlet of base metal sulfides and quartz during the second stage of mineralization. F. Andesite cut by veinlets of galena, sphalerite, and quartz, which represent the second stage of mineralization. Andesite is greenish in color due to pervasive occurrence of epidote.

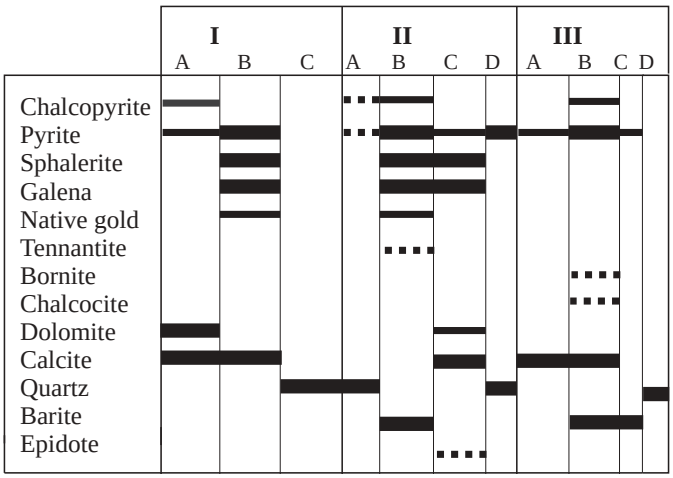

FIG. 7. Mineral parageneses for stages of mineralization in the Gandy deposit. Thick lines show the main minerals, thin lines the accessory minerals, and dashed lines the rare minerals (stages of mineralization are described in text).

are commonly cemented by base metal sulfides, carbonates, and gray microcrystalline quartz (Fig. 6B). Stage I consists of three successive mineral assemblages: (A) dolomite, calcite, chalcopyrite, pyrite; (B) pyrite, native gold, sphalerite, galena, calcite; and (C) microcrystalline quartz. Dolomite in substage A occurs as euhedral to subhedral crystals and calcite occurs as fine-gained aggregates, and chalcopyrite and pyrite are rare. Pyrite in substage B occurs as euhedral to subhedral crystals whereas galena and sphalerite occur as intergrown anhedral crystals. Supergene minerals include goethite, iron oxyhydroxides, malachite, covellite, cerussite, and smithsonite, which replace up to 50 percent of the primary sulfide minerals. Native gold grains occur in goethite and other secondary iron oxides in the oxidized zone (Fig. 6C). The gold grains vary from 20 to 50 μm in size, and they are similar in size and composition to native gold occurring in galena and chalcopyrite (see below).

Stage II: This stage contains high contents of base and precious metals. Narrow veins and veinlets of base metal sulfides, quartz, carbonate, and barite characterize this stage. Vein thicknesses vary from a few centimeters up to 30 cm. On the basis of crosscutting relationships and mineral assemblages, four substages were defined: (A) chalcopyrite, pyrite, and quartz; (B) chalcopyrite, pyrite, tennantite, sphalerite, galena, and barite; (C) pyrite, sphalerite, galena, calcite, dolomite, and rare epidote; and (D) pyrite and microcrystalline quartz. Sphalerite and galena are the main metallic minerals in substage B. Native gold, varying in size from 40 to 70 μm, occurs within chalcopyrite and galena. Pyrite grains in the final stage show a colloform texture which surrounds earlier formed, euhedral pyrite. The supergene assemblage includes cerussite, smithsonite, willemite, covellite, chalcocite, and iron oxyhydroxides, which replace up to 20 percent of primary sulfide minerals.

Stage III: This stage contains low concentrations of gold and comprises veins ranging from 10 to 100 cm in width, with a mineral assemblage of quartz, carbonates, and sulfides such as pyrite and chalcopyrite (Fig. 6D). Finely banded, coarsely banded, comb, crustiform, and breccia textures occur in the veins. This stage consists of four successive mineral associations: (A) calcite and pyrite; (B) pyrite, bornite, chalcocite, chalcopyrite, barite, and calcite; (C) pyrite and barite; and (D) microcrystalline quartz. Although stage III represents a volumetrically major part of the veins, it contains a low concentration of base metals (<1 wt % combined) and Au (<5 g/t). The supergene assemblage in this stage includes malachite and iron oxyhydroxides, which replace up to 20 percent of the primary minerals.

Paragenetic sequence of mineralization at Abolhassani

The mineralogy of the Abolhassani veins consists of base metal sulfides, quartz, and calcite. Like Gandy, the mineralization is divided into three main stages of brecciation, fracture filling, and crustiform banding. On the basis of crosscutting relationships, mineral assemblages, and textures, the main stages of mineralization are divided into several substages (Figs. 6, 8).

Stage I: This is an important stage in terms of base metal content at Abolhassani. It is composed of breccias containing host-rock fragments (Fig. 6E) up to 5 cm in diameter that show propylitic alteration of biotite, hornblende, and pyroxene. The breccias are cemented by base metal sulfides, microcrystalline to fine-grained quartz, calcite, and chlorite. The breccia zones are irregular to tabular in shape and vary from 20 to 30 cm thick. This stage consists of three successive mineral associations: (A) quartz, pyrite; (B) pyrite, chalcopyrite, sphalerite, galena; and (C) quartz, calcite, chlorite. Supergene minerals include covellite, smithsonite, and cerussite.

Stage II: This stage is also important for base metals and is characterized by veins of base metal sulfides (Fig. 6F), quartz, and calcite. Veins vary from 10 to 100 cm thick. This stage consists of four successive mineral assemblages: (A) quartz, pyrite; (B) pyrite, chalcopyrite, sphalerite; (C) pyrite, sphalerite, galena; and (D) quartz, calcite, chlorite. The supergene assemblage includes malachite, covellite, smithsonite, cerussite, and iron oxyhydroxides. Supergene alteration is minor and incipient at Abolhassani and has replaced <10 percent of the primary sulfide minerals.

Stage III: This stage comprises millimeter- to centimeter-thick veinlets of quartz. The veinlets are located on the contact between the hanging wall and footwall of the main veins. The mineral assemblage consists of quartz with fine bands, combs and crustiform textures, and rare pyrite.

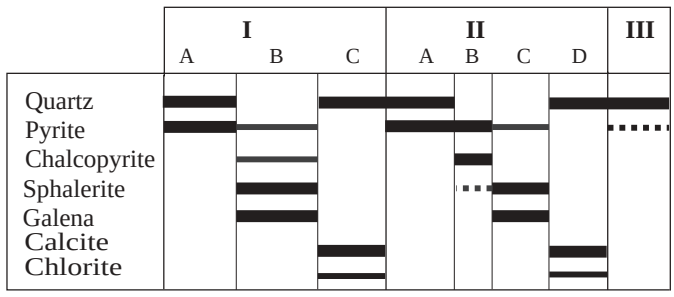

FIG. 8. Mineral parageneses for stages of mineralization in the Abolhassani deposit. Thick lines show the main minerals, thin lines the accessory minerals, and dashed lines the rare minerals (stages of mineralization are described in text).

Supergene effects

Supergene oxidation has affected the gold and base metal mineralization of Gandy above the groundwater table and to a lesser extent at Abolhassani. In the Gandy area, the main supergene minerals are goethite, iron oxyhydroxides, malachite, covellite, cerussite, and smithsonite, which replace 20 to 50 percent of the primary sulfide minerals. The depth of weathering is related to the structure and level of the ground-water table and is about 10 to 20 m below surface in the vicinity of the mine.

The main supergene minerals at Abolhassani are similar to Gandy, including malachite, covellite, smithsonite, cerussite, and iron oxyhydroxides. However, supergene effects are minimal in this area.

Geochemistry and Metal Associations

Chemical compositions of 33 vein samples from Gandy and Abolhassani are listed in Tables 2 and 3. Pearson correlation matrix calculations show that Pb correlates positively with Zn (correlation coefficient, $r = 0.97$), Ag ($r = 0.7$), and Au ($r = 0.65$) in the Gandy area. Gold correlates positively with Ag ($r = 0.94$) and Zn ($r = 0.83$), and As correlates positively with Sb ($r = 0.98$). In the Abolhassani area, Pb correlates positively with Zn ($r = 0.63$) and Ag ($r = 0.61$), and As correlates positively with Sb ($r = 0.65$).

The average (max) assays from 14 channel samples collected across the width (10–100 cm) of the Gandy veins are 14.5 (68.3) g/t Au, 30.6 (161) g/t Ag, 3.1 (13.1) wt percent Pb, 0.84 (3.8) wt percent Zn, and 1.0 (6.3) wt percent Cu (Table 2). The average (max) assays from 19 channel samples (Table 3) across Abolhassani veins (20–100 cm wide) are 0.85 (6.0) g/t Au, 29.5 (115) g/t Ag, 6.4 (16.5) wt percent Pb, 1.2 (5.2) wt percent Zn, and 0.83 (7.7) wt percent Cu.

Geochemical anomalies of wall rock around the veins in the Gandy area were determined over an area of ~1 km^2 (in the southwest corner of Fig. 4). All elements show a log normal distribution and indicate enrichment of Pb, Zn, and Au. The average gold grade in this survey is 0.6 g/t, with a maximum of 43 g/t (Kousari, 2001). Both linear and cluster analysis, not reported here, show positive correlations between As and Au and between Zn and Au. Geochemical distribution maps of elements show overlapping anomalies for Au, As, Zn, Pb, and Cu (Fig. 9) and good spatial correlation with the distribution of exposed veins and alteration zones. The anomalous zones extend from less than 10 to 100 m around the veins (Fig. 9).

Mineral Chemistry

The chemical compositions of native gold, sphalerite, and pyrite were determined by electron probe microanalysis (EMPA), and the average results are listed in Appendix 2.

Native gold

Native gold was found only at Gandy. In stage I, native gold occurs commonly within partially oxidized pyrite and secondary iron oxides such as goethite (Fig. 10A-B). Such gold grains enclosed in iron oxides have a larger size than those in galena and chalcopyrite. In stage II, gold grains coexist with galena, chalcopyrite, and their supergene alteration products, such as cerussite and chalcocite (Fig. 10C-D). No gold grains were found in Abolhassani samples, either during petrographic examination or by EMPA.

Although supergene oxidation was particularly intense in stage I mineralization at Gandy, the gold grains of this stage are likely of hypogene origin. These gold grains (85.1–91 wt % Au) have a composition that is similar to gold grains in unoxidized galena and chalcopyrite from stage II (87.5–91 wt %

TABLE 2. Analyses of Vein, Hydrothermal Breccia, and Wall-Rock Samples from the Gandy Prospect

Sample no.	Latitude	Longitude	Vein width (cm)	Au (ppm)	Ag (ppm)	As (ppm)	Sb (ppm)	Cu (%)	Pb (%)	Zn (%)	Bi (ppm)	Mo (ppm)	Description
Gn-8081	35°19'22"N	54°38'12"E	20	24	NA	468	NA	0.1	2	0.4	7.34	NA	Hydrothermal breccia
Gn-8082	35°19'17"N	54°38'21"E	30	3	NA	1980	NA	2.8	0.1	0.7	3.67	NA	Hydrothermal breccia in tunnel 2
Gn-8083	35°19'19"N	54°38'20"E	40	38.8	59.4	8.7	NA	0.3	13.1	2.8	NA	NA	Hydrothermal breccia in tunnel 3
Gn-8084	35°19'23"N	54°38'20"E	40	1.4	11.9	1420	NA	0.2	0.2	0.1	NA	NA	Hydrothermal breccia
Gn-8085	35°19'27"N	54°38'15"E	30	0.4	1	9.7	NA	0.1	0.4	0.2	NA	NA	Hydrothermal breccia
Gn-8086	35°19'11"N	54°38'1"E	20	4.9	2.4	113	NA	0.5	0.1	0.1	NA	NA	Mineralized vein
Gn-8087	35°19'4"N	54°38'11"E	15	4.7	32.5	38	44	0.1	10.4	2.2	20	8	Mineralized vein
Gn-8088	35°19'19"N	54°38'20"E	20	43.2	154	12200	1120	6.3	5.8	1.5	42	40	Hydrothermal breccia
Gn-8089	35°19'27"N	54°38'15"E	30	68.3	161	64	12	0.4	11.7	3.7	123	32	Mineralized vein
Gn-8090	35°20'34"N	54°38'17"E	30	0.1	<1	NA	NA	0.002	0.002	0.004	NA	NA	Quartz vein
Gn-8091	35°20'27"N	54°38'47"E	15	5.9	2.6	NA	NA	0.4	0.004	0.01	NA	NA	Quartz vein with Py, Ccp
Gn-8092	35°20'11"N	54°38'39"E	20	1.5	2	NA	NA	0.1	0.004	0.02	NA	NA	Quartz vein
Gn-8093	35°19'54"N	54°38'10"E	15	4	1.8	NA	NA	1.1	0.02	0.01	NA	NA	Quartz vein
Gn-8094	35°20'8"N	54°37'50"E	30	2.1	<1	NA	NA	1.1	0.02	0.01	NA	NA	Quartz-carbonate vein
Gn-8095	35°19'16"N	54°37'49"E	Wall rock	0.1	NA	13.3	NA	0.03	0.02	0.02	0.27	2.5	Altered tuff
Gn-8096	35°20'16"N	54°39'6"E	Wall rock	0.1	NA	26	NA	0.02	0.01	0.1	0.5	1.5	Altered tuff
Gn-8097	35°20'4"N	54°37'58"E	Wall rock	0.1	<1	<20	<10	0.02	0.01	0.01	<10	4	Altered Andesite

Notes: Vein samples were collected across the full width of veins by 3- to 5-cm-wide channel samples, whereas the wall rock was chip sampled; the samples were analyzed at the Geological Survey of Iran; techniques used: fire assay or atomic absorption spectrometer for Au, ICP-AES for Ag, As, Sb, Cu, Zn, and Bi, and atomic absorption spectrometer for Pb and Mo; Ccp = chalcopyrite, Py = pyrite; NA = not analyzed

TABLE 3. Analyses of Vein and Wall-Rock Samples from the Abolhassani Prospect

Sample no.	Latitude	Longitude	Vein width (cm)	Au (ppm)	Ag (ppm)	As (ppm)	Sb (ppm)	Cu (%)	Pb (%)	Zn (%)	Bi (ppm)	Mo (ppm)	Description
Ab-7081	35°21'28"N	54°37'41"E	30	0.1	14.7	23	11	0.1	9.2	4.2	<10	4	Qtz-Gn vein, tunnel 1
Ab-7082	35°21'28"N	54°37'41"E	50	0.1	107	22	14	0.6	11.9	5.2	230	16	Qtz-Gn vein, tunnel 1
Ab-7083	35°21'28"N	54°37'41"E	20	0.6	<1	27	36	0.5	4.1	0.1	<10	8	Qtz vein, tunnel 1
Ab-7084	35°21'29"N	54°38'10"E	50	0.6	115	27	<10	0.02	6.7	0.4	<10	2	Qtz-Gn vein, tunnel 2
Ab-7085	35°21'29"N	54°38'10"E	30	2	24.3	23	<10	0.1	15.1	1	<10	4	Qtz-Gn vein, tunnel 2
Ab-7086	35°21'29"N	54°38'10"E	30	0.5	21.6	20	<10	0.2	6.7	1.2	<10	4	Qtz-Gn vein, tunnel 2
Ab-7087	35°21'29"N	54°38'10"E	30	0.2	5	<20	<10	0.1	4.1	0.05	<10	4	Qtz-Gn vein, tunnel 2
Ab-7088	35°21'29"N	54°38'10"E	Chip	0.4	65.1	64	25	7.7	2.1	0.1	53	2	Gn, Ccp, Py, Qtz, tunnel 2
Ab-7089	35°21'29"N	54°38'10"E	50	0.7	<1.0	20	<10	0.01	2	0.7	<10	4	Qtz vein, tunnel 2
Ab-7090	35°21'29"N	54°38'10"E	30	1.1	7.4	20	<10	0.03	4.4	0.8	<10	4	Qtz vein, tunnel 2
Ab-7091	35°21'54"N	54°38'9"E	20	0.1	1.5	42	90	2.6	0.01	0.001	<10	4	Qtz vein with some Py, Ccp
Ab-7092	35°22'4"N	54°37'22"E	50	0.1	<1	<20	<10	0.01	0.003	0.004	<10	56	Qtz vein
Ab-7093	35°21'54"N	54°38'9"E	30	6	NA	7.9	NA	1.2	0.001	0.01	375	NA	Qtz vein
Ab-7094	35°21'28"N	54°37'41"E	50	0.7	27	NA	NA	0.3	15.1	2.1	NA	NA	Qtz-Gn vein, tunnel 1
Ab-7095	35°21'28"N	54°37'41"E	30	0.8	11.1	NA	NA	0.1	4.6	2.3	NA	NA	Qtz-Gn vein, tunnel 1
Ab-7096	35°21'28"N	54°37'41"E	100	0.7	37	NA	NA	1.2	6.8	0.4	NA	NA	Qtz-Gn vein, tunnel 2
Ab-7097	35°21'28"N	54°37'41"E	100	0.2	54.7	NA	NA	0.7	6.9	0.5	NA	NA	Qtz-Gn vein, tunnel 2
Ab-7098	35°21'28"N	54°37'41"E	50	0.7	48.5	NA	NA	0.1	16.5	1.1	NA	NA	Qtz-Gn vein, tunnel 2
Ab-7099	35°21'28"N	54°37'41"E	50	0.6	18.7	NA	NA	0.1	6.2	2.2	NA	NA	Qtz-Gn vein, tunnel 2
Ab-70100	35°21'28"N	54°37'41"E	Wall rock	0.003	<1	20	26	0.03	0.01	4.9	<10	2	Altered andesite, tunnel 2
Ab-70101	35°21'52"N	54°38'32"E	Wall rock	0.4	NA	6.8	NA	1.2	0.002	0.02	2.9	NA	Altered andesite stained by malachite
Ab-70102	35°21'50"N	54°38'38"E	Wall rock	0.1	NA	14.1	NA	0.02	0.01	0.03	<10	NA	Altered andesite

Notes: Samples were analyzed by Geological Survey of Iran; techniques used: fire assay or atomic absorption for Au, inductively coupled plasma spectroscopy for Ag, As, Sb, Cu, Zn, and Bi, and atomic absorption for Pb and Mo; most veins sampled across their full width by a 3- to 5-cm-wide channel, except for chip samples, as noted; wall rocks were also chip sampled; Ccp = chalcopyrite, Gn = galena, Py = pyrite, Qtz = quartz; NA = not analyzed

Au; Appendix 2a). This suggests that the gold grains hosted by goethite are hypogene and were not affected during supergene oxidation of pyrite. In the Gandy area, relief is low, the climate is now arid (annual rainfall <150 mm), and the vegetation is sparse. Under these conditions, gold and silver mobility in the weathering environment is limited (Webster and Mann, 1984).

Sphalerite

Sphalerite crystals and aggregates in the Gandy veins display subtle color zoning. Cores of sphalerite grains range from clear to light yellow, changing to yellow toward their rims. The FeS and CdS contents range from 0.8 to 1.6 and 0.2 to 0.6 mol percent (Appendix 2b), respectively, and increase slightly from core to rim. Sphalerite contains blebs of chalcopyrite.

In the Abolhassani area, sphalerite crystals do not display any color zoning. Their FeS content ranges from 1 to 2.9 mol percent (Appendix 2b). Sphalerite contains blebs of chalcopyrite and also occurs as fine inclusions (20–50 μm) within galena (Fig. 10E). The FeS content of these inclusions is 0.2 mol percent, much lower than other sphalerite grains. The CdS contents of both types of sphalerite range from 0.15 to 0.32 wt percent, averaging approximately 0.2 mol percent.

Pyrite

Two types of pyrite have been documented in stage II of Gandy mineralization. The first type is characterized by euhedral to subhedral crystals that are disseminated throughout the ore. These pyrite grains are As poor (<0.02 wt %) and are commonly found in association with chalcopyrite, sphalerite, and galena. The second type is characterized by a colloform texture, which occurs most commonly as overgrowths on small (20–50 μm) euhedral pyrite crystals. The overgrowths vary in thickness from 5 to 30^{+} μm. Within the rims, the highest As concentrations (up to 6.4 wt %, Appendix 2c) were detected in the outermost growth zone, which is brighter than the rest of the rims in the backscattered electron images. These concentrations compare with low As concentration (<0.02 wt %) in the euhedral pyrite cores (Fig. 10F-G). In this study, gold was not detected in the arsenian pyrite samples, although EMPA detection limit is quite high (about 300 ppm Au).

A strong correlation between Au and As in arsenian pyrite has been noted in sediment-hosted gold deposits (Bakken et al., 1991; Arehart et al., 1993) but not from epithermal veins hosted by volcanic rocks. Nevertheless, it appears that a portion of the gold may be associated with arsenian pyrite in this district. Gold is typically incorporated into pyrite by chemisorption onto As-rich, Fe-deficient growth surfaces (Fleet et al., 1993; Fleet and Mumin, 1997). The amount of gold that can enter arsenian pyrite is probably a function of the amount of arsenic present, as well as the crystallographic position and distribution of arsenic in the pyrite structure (Simon et al., 1999).

In the Abolhassani area, euhedral to subhedral pyrite grains do not display zoning. The pyrite is mostly As poor (Appendix

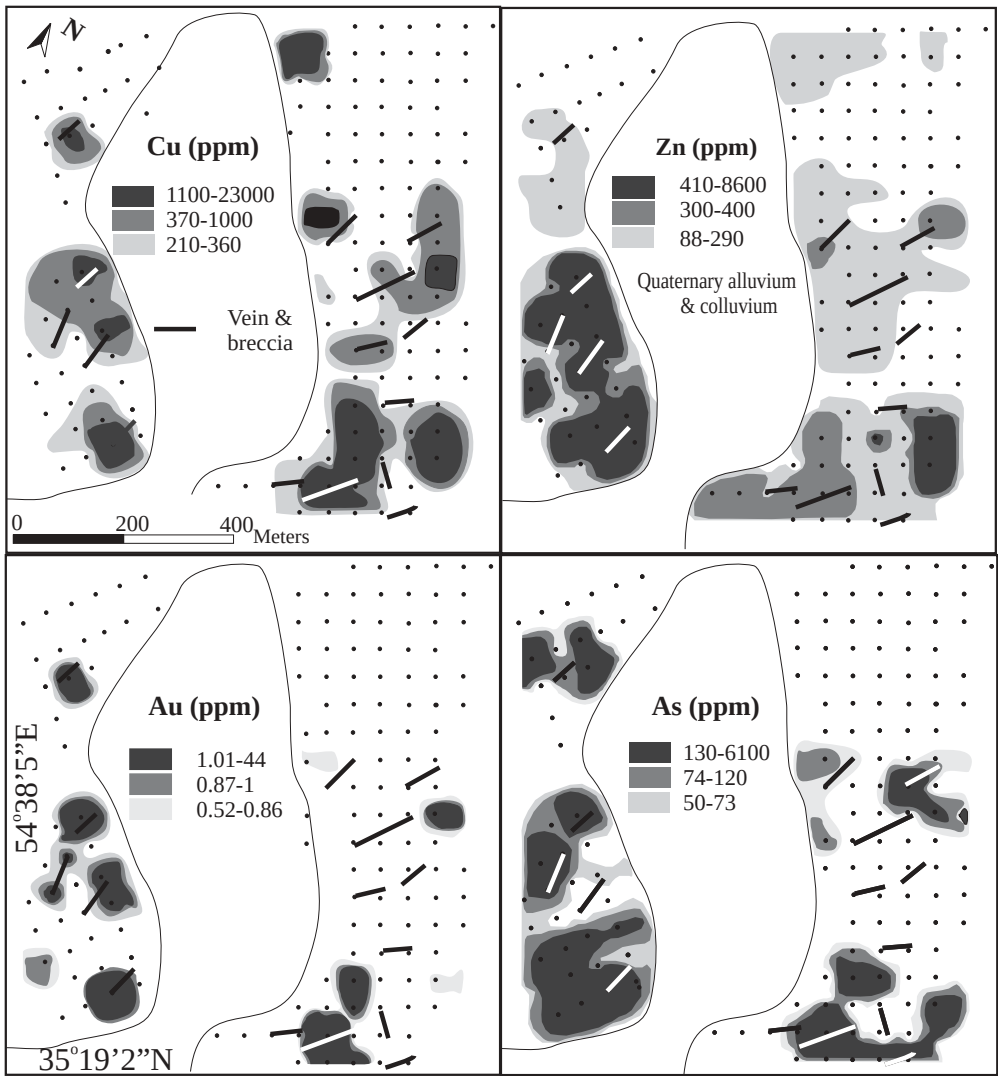

FIG. 9. Lithogeochemical anomaly maps of Au, As, Cu, and Zn for the southwestern portion of the Gandy prospect; the central area is covered by Quaternary sediments. Vein and breccia locations are shown by solid lines. Sampling locations are shown as small solid circles in the diagram.

2c). A high concentration of As was detected in only one pyrite grain, ranging from 0.2 to 1.9 wt percent (Fig. 10H).

Fluid Inclusion Data

Fluid inclusion data were collected from Gandy and Abolhassani to characterize and compare the fluid temperatures and compositions. Fluid inclusions in quartz crystals are very small and only a few were selected for study, whereas sphalerite contains inclusions suitable for study. Most data were obtained from six doubly polished sections (70 μm thick) of subhedral sphalerite crystals, which range from 2 mm to 1 cm in size. The size of fluid inclusions ranges from 5 to 40 μm, with maximum sizes up to ~120 μm in elliptical, irregular, and rod shapes. Primary, pseudosecondary, and secondary inclusions were identified, and these are mostly liquid rich and aqueous with no daughter minerals. All inclusions are two phase at room temperature (liquid and vapor), with vapor to liquid ratios ranging between 0.1 and 0.4. Vapor-rich secondary inclusions were found in three samples, and they coexist with liquid-rich inclusions, although necking phenomena are suspected in these samples because some liquid-rich or liquid-only inclusions were found adjacent to vapor-rich inclusions.

Primary fluid inclusions occur in growth zones parallel to crystal faces, as solitary inclusions or as isolated assemblages of inclusions. The latter are randomly distributed. Pseudosecondary inclusions occur along planes crosscut by later growth zones. The growth zones in sphalerite are distinguished by color variations, from yellow to clear, and by numerous very small primary fluid inclusions which define former crystal surfaces.

Microthermometric studies were carried out by conventional techniques using a FLUID INC.-adapted U.S. Geological Survey gas-flow heating-freezing system with precisions of ±1° and ±0.1°C for temperatures of homogenization and ice melting, respectively. The results are summarized in Appendices 3 and 4. Each line of fluid inclusion data in these

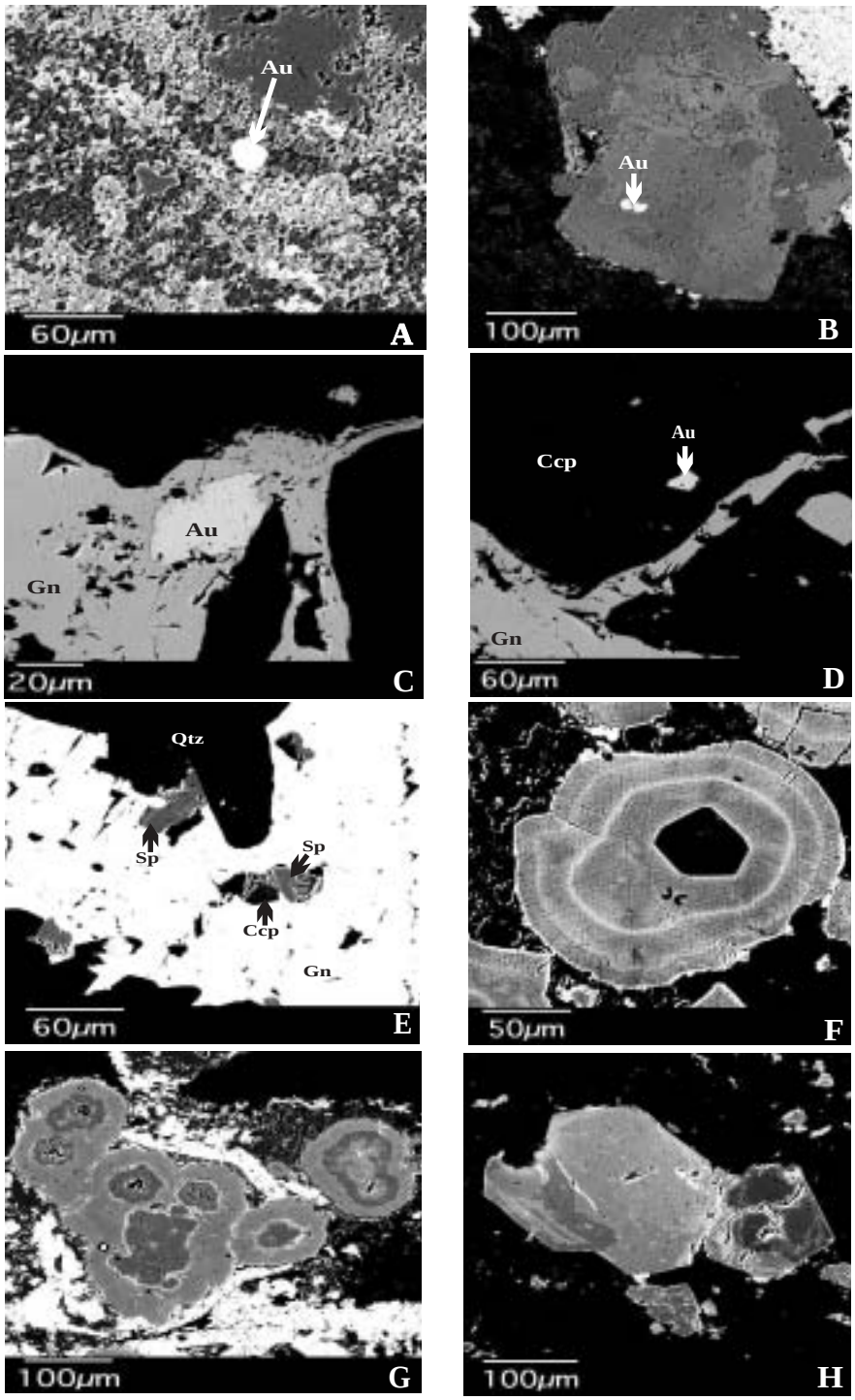

FIG. 10. Backscattered electron images of minerals from the Gandy and Abolhassani prospects. A. and B. Gold grains (Au) in secondary iron oxides of stage I (Gandy prospect). C. and D. Gold within galena (Gn) and chalcopyrite (Ccp) of stage II (Gandy prospect). E. Sphalerite (Sp) within galena of stage I (Abolhassani prospect). F. and G. Compositional zoning of pyrite of stage II (Gandy prospect); the bright bands contain up to 6.4 wt percent As. H. Weakly zoned, As-poor pyrite from Abolhassani.

Appendices represents measurements along individual planes or in groups of inclusions having constant vapor to liquid ratios and that yielded consistent data. Such populations of fluid inclusions are termed fluid inclusion assemblages, and these provide the most reliable data sets (Goldstein and Reynolds, 1994). Homogenization and ice-melting temperatures were obtained for 524 and 44 fluid inclusions, respectively, representing 94 fluid inclusion assemblages in the six samples.

Gandy veins

Fluid inclusion data were obtained from three different veins in stage II to determine the spatial variations over the period of mineralization. Sample locations are shown in Figure 4. These samples were collected from mineralized veins about 200 m apart but at the same elevation. The average homogenization temperature (T_h) of primary inclusions in fluid inclusion assemblages ranges from 234° to 285°C (Fig. 11, Appendix 3), with a single peak at about 250°C. Three vapor-rich inclusions were found with a T_h of more than 300°C and necking is suspected. Within individual color zones of sphalerite the homogenization temperatures are similar, but the average temperature decreases from cores to rims in individual crystals. Ice-melting temperatures ($T_{m(ice)}$) of fluid inclusions range from –2.6 to –3.3°C. Salinities were calculated from ice-melting temperatures, using the equations of Bodnar (1993), and range from 4.2 to 5.4 wt percent NaCl equiv. T_h and $T_{m(ice)}$ values decrease from sample 79/H59 to 79/H51 and Ga-M-3 along a simple linear trend (Fig. 12).

Abolhassani veins

Fluid inclusion data were obtained from three different veins, with sample locations shown in Figure 5. The average T_h of primary inclusions in fluid inclusion assemblages ranges from 233° to 340°C (Fig. 11, Appendix 4), with three peaks in the data at about 250°, 275°, and 340°C. Homogenization temperatures are consistent for individual fluid inclusion assemblages, indicating that these multiple histogram peaks are meaningful. Ice-melting temperatures and salinities of fluid inclusions range from –4.2 to –15.6°C and 6.7 to 18.7 wt percent NaCl equiv, respectively. T_h versus $T_{m(ice)}$ measurements show a large variation, even within a single sample, but values vary along a simple linear dilution trend (Fig. 12).

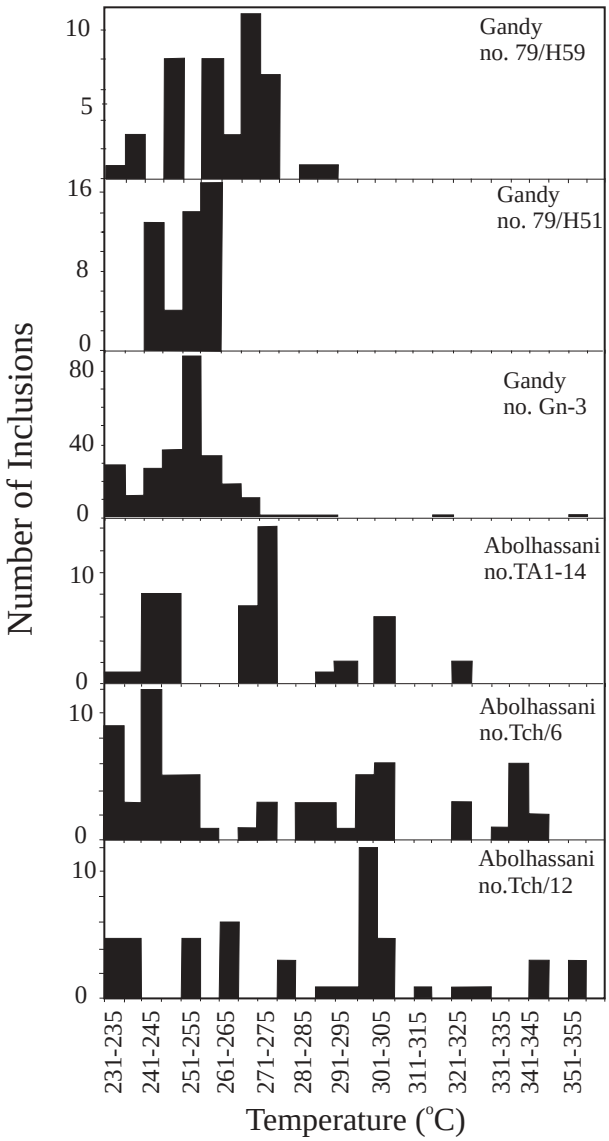

FIG. 11. Frequency histograms of homogenization temperatures (T_h) of sphalerite-hosted primary fluid inclusions in internally consistent fluid inclusion assemblages from the Gandy and Abolhassani prospects.

Sulfur Isotope Data

Sulfur isotope data were obtained for two samples from Gandy and three samples from Abolhassani (Table 4). The sample locations were the same as those selected for fluid inclusion work.

The temperatures estimated from isotope compositions of coexisting sulfide minerals rely on the following assumptions: (1) isotopic equilibrium was established between the two minerals, (2) the isotopic composition did not change by post-depositional isotope exchange with sulfur in other minerals or fluids, and (3) the separated mineral phases were pure (Faure, 1986). Sphalerite-galena and barite-galena pairs were used here, employing the fractionation factors compiled by Ohmoto and Goldhaber (1997). The calculated isotopic temperatures are given in Table 4.

In the Gandy district, the calculated isotopic equilibration temperatures for sphalerite and galena pairs (236° and 245°C) are in good agreement with homogenization temperatures of fluid inclusions (249° and 262°C for the two samples, respectively). The range of temperatures (including

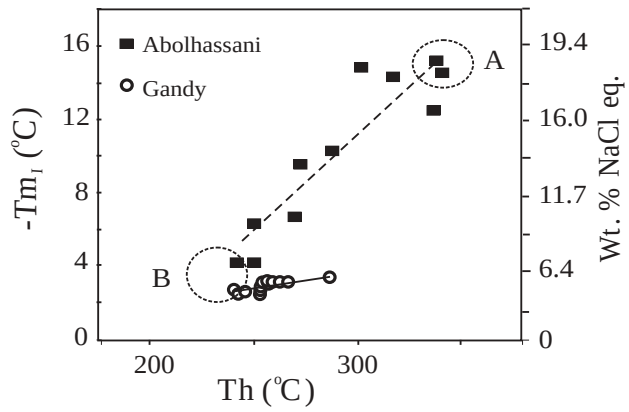

FIG. 12. Homogenization (T_h) vs. ice-melting ($T_{m(ice)}$) temperatures for fluid inclusion assemblages from the Gandy and Abolhassani prospects. Comparison of average T_h and $T_{m(ice)}$ values for the two deposits indicates the presence of a similar, moderate-salinity fluid in both deposits at a similar temperature (fluid B), whereas there was also a higher salinity component (fluid A) present at times in Abolhassani, evidence for intermittent injection of a mineralizing brine that was subsequently diluted.

TABLE 4. Sulfur Isotope Composition of Coexisting Sphalerite, Galena, and Barite in the Sulfide Ores

Sample no.	Latitude	Longitude	Mineral	$\delta^{34}S_{CDT}$ (‰)	$\Delta^{34}S_{Sph\text{-}Gn}$	$T_{Sph\text{-}Gn}$ (°C)	$\Delta^{34}S_{Bar\text{-}Gn}$	$\delta^{34}S_{H_2S}$ (‰)	$T_{Bar\text{-}Gn}$ (°C)	T_h (°C) (low/mean/high)
Gandy district										
80/HG20	35°19'18"N	54°37'48"E	Barite	+16.0 ± 0.1						
			Sphalerite	–4.3 ± 0.1	2.8	236 ± 9	23.1	–5.1 ± 0.1	293 ± 2	243/249/258
			Galena	–7.1 ± 0.1						
80/HG21	35°19'30"N	54°37'55"E	Barite	+ 15.9 ± 0.1						
			Sphalerite	–3.3 ± 0.1	2.7	245 ± 9	21.6	–4.2 ± 0.1	313 ± 2	233/262/287
			Galena	–6.0 ± 0.1						
Abolhassani district										
Tch/6	35°19'28"N	54°37'41"E	Sphalerite	–3.8 ± 0.1	–0.5					233/275/337
			Galena	–3.3 ± 0.1						
Tch/19	35°19'28"N	54°37'41"E	Sphalerite	–4.4 ± 0.1	1.7	381 ± 20				236/280/354
			Galena	–6.1± 0.1						
TA1/14	35°19'29"N	54°38'10"E	Sphalerite	–2.8 ± 0.1	1.3	472 ± 30				234/270/322
			Galena	–4.1 ± 0.1						

Notes: Calculated isotopic temperatures from fractionation factors in Ohmoto and Goldhaber (1997); homogenization temperatures (T_h) listed for comparison

uncertainties) from the two methods overlaps, with a variation in the mean temperatures of 15°C. The isotopic temperatures from barite-galena pairs are higher (293° and 313°C) than the corresponding temperatures of homogenization of fluid inclusion assemblages. Sphalerite-galena pairs do not give reasonable isotopic equilibration temperatures in the Abolhassani samples, and in one case (sample Tch/6), $\delta^{34}S_{Sph\text{-}Gn}$ is negative (Table 4). The isotopic temperatures are 100° and 200°C higher than the ~275°C mean for T_h, although the range of homogenization temperatures of fluid inclusions is as high as 354°C (Appendix 4). These discrepancies suggest that sphalerite and galena did not coprecipitate.

Discussion

Composition of fluids

Fluid inclusions from gold-rich epithermal environments are generally two-phase liquid and vapor (Roedder, 1984; Bodnar et al., 1985) and have small freezing point depressions (Hedenquist and Henley, 1985), indicating salinities <1 to 2 wt percent NaCl equiv. By contrast, those from silver- and base metal-rich deposits have higher salinity, with evidence for pulses of much higher salinity. For example, at Fresnillo (Simmons et al., 1988) and other Mexican deposits (Albinson et al., 2001), salinities vary from ~5 to 20 wt percent NaCl equiv or higher. Salinity determinations indicate that sphalerite-hosted fluid inclusions from the Gandy veins are more dilute than similar fluid inclusions from the Abolhassani veins. Clathrates (Collins, 1979) were not observed in any of the freezing runs. However, Hedenquist and Henley (1985) noted that up to –1.5°C of the freezing point depression in epithermal fluid inclusions could be due to the presence of up to 4 wt percent dissolved CO_2 without clathrate formation during freezing. If CO_2 is present, the salinities indicated in this study represent maximum values and could be up to ~2.6 wt percent NaCl equiv lower (however, this will not affect the interpretation here).

The salinities of inclusions are consistent with metal contents and mineralogical data from the two areas. The Abolhassani samples have higher average Ag/Au ratios (~35) and higher Pb + Zn contents (avg 7.6 wt %) than those from Gandy (Ag/Au ratios of 2 and avg 3.9 wt %, respectively; Fig. 13), consistent with the significantly higher (~4×) maximum salinity at Abolhassani (18.7 wt %) compared to Gandy (5.4 wt %). Such a relationship between silver and base metal ores with relatively higher salinities and gold-silver ores with lower salinities has been previously noted (Henley, 1985) and confirmed for Mexican epithermal deposits (Simmons et al., 1988; Simmons, 1991; Albinson et al., 2001).

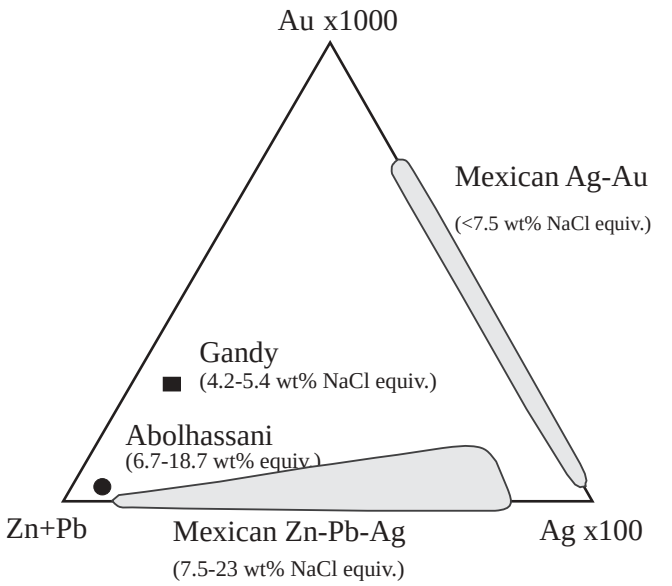

FIG. 13. Ternary diagram of relative precious and base metal contents of the Gandy and Abolhassani deposits (averages of veins from Tables 2 and 3, respectively). Ranges for Mexican epithermal deposits are shown for comparison (fields from Albinson et al., 2001).

Silver and base metal transport in the epithermal environment is dominated by chloride complexes (Seward and Barnes, 1997). These complexes are more important for silver and base metal transport than for gold transport under the relatively reduced, neutral pH conditions (Seward and Barnes, 1997) that characterized the epithermal systems of Gandy and Abolhassani. In contrast, the $Au(HS)_2^-$ bisulfide complex is most important for gold transportation in this epithermal environment (Benning and Seward, 1996; Seward and Barnes, 1997), and thus gold transport is not affected by salinity in the same way as silver and base metal transport.

Comparison of T_h versus $T_{m(ice)}$ measurements for the two deposits (Fig. 12) indicates the presence of a similar, moderate-salinity fluid in both deposits at a similar temperature (~250°C, 5 wt % NaCl equiv; fluid B), whereas there was also a higher salinity component present at times in the Abolhassani deposit. This was most likely caused by intermittent pulses of higher temperature, high-salinity fluid (~340°C, 18 wt % NaCl equiv; fluid A), as recorded during the growth of individual crystals (e.g., sample Tch-6, Appendix 4).

Ore deposition and depths of formation

Boiling and mixing are the two principal physical processes affecting mineral deposition in geothermal systems (Giggenbach and Stewart, 1982). Boiling occurs in the upflow of most high permeability systems, whereas linear thermal profiles are common on the margins (due to mixing or low permeability; Hedenquist et al., 1992). In the Gandy area, the presence of hydrothermal breccias in stage I with gold and base metal mineralization is evidence for periods of sharp pressure drops. These may have led to at least intermittent boiling in this system. However, fluid inclusion data from sphalerite grains of stage II show a dilution trend for the ore-forming fluids (Fig. 12). T_h and $T_{m(ice)}$ of sphalerite grains are similar in individual zones and consistently decrease from cores to rims in individual grains. This fact and the relationship between T_h and $T_{m(ice)}$ underscore the importance of relatively small amounts of cooling as the result of dilution during base metal mineralization of stage II.

The relationship between fluid inclusion T_h and $T_{m(ice)}$ data (Fig. 12) from the Abolhassani district clearly shows a trend of strong dilution, evidence that a hot, saline fluid mixed with a cooler, more dilute fluid. Considering the paragenetic sequence of mineralization, and the systematic variation of T_h and $T_{m(ice)}$ between fluid inclusion assemblages in individual crystals of sphalerite from the Abolhassani district, it appears that the high-salinity fluid was periodically injected and mixed with lower salinity fluid over short periods of time. The main mechanism of base metal mineralization at Abolhassani may have been the mixing of such brines with the more dilute solutions, although the lack of fluid inclusion evidence for boiling does not preclude this mechanism. Indeed, the presence of hydrothermal breccias, microcrystalline quartz, and crustiform banded quartz suggest that boiling conditions may have existed at some intervals during the evolution of this hydrothermal system.

The highest range of homogenization temperatures (320°–350°C, with a peak at 340°C) at Abolhassani is difficult to explain at epithermal depths under hydrostatic pressure. T_h data are consistent in individual fluid inclusion assemblages; no evidence of necking down was observed for these samples. Thus, the high-temperature inclusions are not artifacts but record influxes of a high-temperature fluid in this hydrothermal system. Such a high-temperature fluid probably existed at deeper levels in the system and may reflect a hydrothermal regime associated with changes from hydrostatic toward lithostatic pressure (cf. Arribas et al., 1995). The common occurrence of quartz breccias in the Abolhassani district indicates that the fluid pressure probably increased periodically. High-pressure conditions are not characteristic of steady-state hydrothermal activity (Simmons, 1991) but may have been caused by self-sealing at shallow levels due to mineral deposition or associated with magma ascent from depth (Simmons, 1991). When the permeability barrier was broken, the pressure dropped rapidly and the high-temperature (~340°C) fluid was quenched by mixing with the lower temperature (~250°C) fluid, depositing base metal sulfides. This process was repeated at least two times, as suggested by the observed paragenetic sequence.

The depth of formation below the paleowater table can be estimated from hydrostatic boiling point curves (Haas, 1971), assuming hydrostatic pressure. However, because of the lack of evidence for boiling, such an estimate will provide a minimum value. The Gandy 250°C, 5 wt percent data were fitted to the 5 wt percent calculated boiling curve. In the case of Abolhassani, the average temperature of the second group in the histogram, which represents an intermediate 270°C, ~10 wt percent salinity fluid (Fig. 12), was fitted to the 10 wt percent calculated boiling curve (Fig. 14); if the lower temperature data were used, the result would be similar to Gandy. The 20 wt percent boiling curve is also shown for reference, as this is close to the maximum salinity found at Abolhassani. In both districts mineralization occurred at moderate epithermal depths based on these average fluid compositions, with the present surface at a respective minimum of ~430 and ~600 m below the paleowater table for the modeled Gandy and Abolhassani data.

Paleodepths of ~500 m are characteristic of silver- and base metal-rich epithermal systems of the intermediate-sulfidation category (Hedenquist et al., 2000; Albinson et al., 2001). In both areas considered here it is possible that mineralized veins existed at shallower depths and have now been eroded. The present surface at Abolhassani may represent a deeper level than Gandy, consistent with the higher Ag/Au ratios and higher base metal contents at Abolhassani, both of which typically increase with increasing depth in epithermal deposits (Buchanan, 1981). Also, Abolhassani has less oxidation at its present higher elevation, suggesting that the oxidized zone may have been mostly eroded. The average temperatures in the two areas, as well as the sulfidation state as indicated by sulfide assemblage and FeS compositions of sphalerite, are typical of the Ag-Au and base metal style of intermediate-sulfidation epithermal mineralization (Einaudi et al., 2003) noted elsewhere, e.g., in Mexico and Nevada (Albinson et al., 2001; John, 2001).

In summary, base metal-rich mineralization of the Abolhassani deposit appears to have been caused by the periodic introduction of a high-salinity fluid, with clear evidence for mixing between this fluid and a moderate-salinity end member similar to that present at Gandy. Similar evidence for the

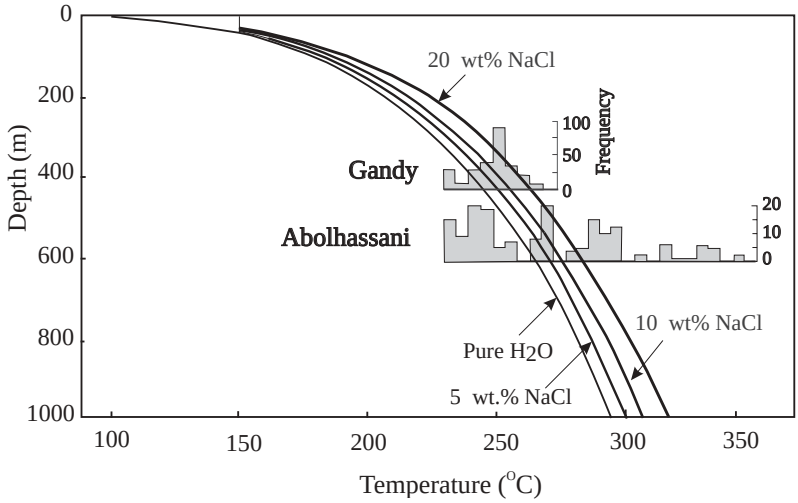

FIG. 14. Histograms of fluid inclusion data from Gandy (sample GN-3) and Abolhassani (all samples) plotted on boiling point for depth curves of H_2O–NaCl (5 and 10 wt % NaCl equiv, respectively). The curves of pure H_2O and 20 wt percent NaCl are shown for reference (from Haas, 1971). Gandy data were fitted at the mean T_h values to the 5 wt percent NaCl curve, whereas the intermediate histogram from Abolhassani (Fig. 11) was fitted to the 10 wt percent NaCl curve, as appropriate for measured salinities.

presence of lower and higher salinity fluids in the same deposit has also been noted previously for silver and base metal mineralization in the Fresnillo district (Simmons et al., 1988; Simmons 1991) and in other intermediate-sulfidation epithermal deposits of Mexico (Albinson et al., 2001). Such high-salinity brines may evolve in a magmatic environment (Simmons, 1991; Albinson et al., 2001).

Summary and Conclusions

Mineralization in the Gandy area occurred in three main stages, the first two being economically important in terms of precious and base metal mineralization. The final stage is dominated by quartz and calcite. The high gold grades at Gandy (up to 68 g/t) appear to be hypogene in origin, as supergene effects are limited. Mineralization of the Abolhassani veins also occurred in three main stages. The first two stages contain similar mineral assemblages, including quartz, calcite, galena, sphalerite, and pyrite, whereas the final stage is dominated by quartz and calcite. This district is dominated by base metal mineralization and gold grades are relatively low in the veins.

The average homogenization temperature of fluid inclusion assemblages has a peak at about 250° for Gandy and three peaks at about 250°, 275°, and 340°C for Abolhassani. Homogenization and ice-melting point data indicate dilution trends for both districts, with a common fluid of about 5 wt percent NaCl equiv present in both systems. In addition, a brine with a maximum salinity of about 18.7 wt percent NaCl equiv was present periodically in the Abolhassani hydrothermal system.

The minimum depth of formation was about 430 and 600 m below the paleowater table for Gandy and Abolhassani, respectively. However, Abolhassani is presently at an elevation 200 m higher than Gandy, indicating a minimum of 370 m of uplift relative to Gandy, and possibly more, as the result of tectonic activity. Alternatively, the volcanic landforms may have had significant relief, with Abolhassani forming originally at a higher elevation (and closer to the vent area?) than Gandy.

Precious and base metal mineralization within hydrothermal breccias of the Gandy district may have deposited under boiling conditions, whereas base metal mineralization in stage II occurred as the result of dilution. Base metal sulfides within the Abolhassani veins were deposited during periodic injection of high-temperature metalliferous brines at pressures greater than hydrostatic. Dilution was the main precipitation mechanism at Abolhassani.

Exploration implications

The Gandy area contains a gold-silver base metal epithermal deposit, locally with bonanza gold grades in veins, and appears to have greater economic potential than the Abolhassani area. Based on the characteristics of mineralization at Abolhassani, with its lower grades of gold and high-salinity fluid, the presence of higher grade precious metal zones at greater depth is unlikely. By contrast, Gandy may have potential at depth for extensions of the high-grade gold veins. Exploration in the region should focus on areas with geologic evidence for relatively little posthydrothermal erosion, <200 to 300 m beneath the paleosurface, thus increasing the preservation potential for epithermal veins with high gold grades similar to those at Gandy.

The mineralogy of ore, gangue, and alteration products, combined with fluid inclusion data from both areas, indicate that these are intermediate-sulfidation epithermal veins that share characteristics with those of major districts in Mexico, western United States, Peru, and elsewhere. The presence of geochemical anomalies and many ore showings and abandoned mines (Fig. 1) with similar epithermal characteristics suggests that the Torud-Chah Shirin mountain range is prospective for precious and base metal epithermal deposits. In particular, areas of little erosion may have unappreciated

potential at depth for high-grade gold veins, particularly where there is evidence for the presence of relatively low salinity hydrothermal systems. In addition, the presence of other types of deposits indicates that this region is also prospective for a variety of styles of volcanic-hosted mineralization, depending on the level of erosion. Much of the epithermal mineral potential of this arc, and adjacent regions, remains untested.

Acknowledgments

We are sincerely grateful to the management of the Geological Survey of Iran, in particular M.T. Korehei and S. Kousari, for providing support in the field. Saeed Alirezaei gave timely advice and encouragement throughout many parts of this investigation, and Bahram Daneshfar (University of Ottawa) provided advice on the lithogeochemical presentation. Peter Jones (Carleton University) assisted with the electron probe work, and Wendy Adi (University of Ottawa) assisted with stable isotope analysis. We thank Ron Hartree for XRF analysis (University of Ottawa), and Kambeaz Tahieri and George Mrazek for their help with the preparation of polished thin and doubly polished sections. We thank J. Lang and S. Turner for their helpful reviews of the paper.

This paper is part of a Ph.D. study by the senior author at the University of Shahid Beheshti, sponsored by the Ministry of Science, Research, and Technology of Iran, and much of analytical work was carried out while the senior author was an exchange Ph.D. student at the University of Ottawa. The support for the work was supplied by research grants to KHH from the Natural Science and Research Council of Canada.

July 26, 2002; January 30, 2004

REFERENCES

Alavi, M., 1991, Tectonic map of the Middle East (scale 1:5,000,000): Geological Survey of Iran.

——1996, Tectonostratigraphic synthesis and structural style of the Alborz mountain system in northern Iran: Journal of Geodynamics, v. 21, p. 1–33.

Albinson, T., Norman, D.I., Cole, D., and Chomiak, B., 2001, Controls on formation of low-sulfidation epithermal deposits in Mexico: Constraints from fluid inclusion and stable isotope data: Society of Economic Geologists Special Publication 8, p. 1–32.

Arehart, G.B., Chryssoulis, S.L., and Kesler, S.E., 1993, Gold and arsenic in iron sulfides from sediment-hosted disseminated gold deposits: Implications for depositional processes: Economic Geology, v. 88, p. 171–185.

Arribas, A., Jr., Cunningham, C.G., Rytuba, J.J., Rye, R.O., Kelly, W.C., Podwysocki, M.H., McKee, E.H., and Tosdal, R.M., 1995, Geology, geochronology, fluid inclusions, and isotope geochemistry of the Rodalquilar gold alunite deposit, Spain: Economic Geology, v. 90, p. 795–822.

Bakken, B.M., Fleming, R.H., and Hochella, M.F., Jr., 1991, High-resolution microscopy of auriferous pyrite from the Post deposit, Carlin district, Nevada: Minerals, Metals, and Materials Society, Process Mineralogy XI, p. 13–23.

Benning, L.G., and Seward, T.M., 1996, Hydrosulfide complexing of Au(I) in hydrothermal solutions from 150 to 400°C and 500 to 1500 bars: Geochimica et Cosmochimica Acta, v. 60, p. 1849–1871.

Bodnar, R.J., 1993, Revised equation and table for determining the freezing point depression of H_2O-NaCl solutions: Geochimica et Cosmochimica Acta, v. 57, p. 683–684.

Bodnar, R.J., Reynolds, T.J., and Kuehn, C.A., 1985, Fluid inclusion systematics in epithermal systems: Reviews in Economic Geology, v. 2, p. 73–97.

Buchanan, L.J., 1981, Precious metal deposits associated with volcanic environments in the Southwest: Arizona Geological Society Digest 14, p. 237–262.

Collins, P.L.F., 1979, Gas hydrate in CO_2-bearing fluid inclusions and the use of freezing data for estimation of salinity: Economic Geology, v. 74, p. 1435–1444.

Cooke, D.R., and Simmons, S.F., 2000, Characteristics and genesis of epithermal gold deposits: Reviews in Economic Geology, v. 13, p. 221–244.

Einaudi, M.T., Hedenquist, J.W., and Inan, E., 2003, Sulfidation state of hydrothermal fluids: The porphyry-epithermal transition and beyond: Society of Economic Geologists and Geochemical Society Special Publication 10, p. 285–313.

Faure, G., 1986, Principles of isotope geology, 2nd ed.: New York, John Wiley and Sons, 541 p.

Fleet, M.E., and Mumin, A.H., 1997, Gold-bearing arsenian pyrite and marcasite and arsenopyrite from Carlin trend gold deposits and laboratory synthesis: American Mineralogist, v. 82, p. 182–193.

Fleet, M.E., Chryssoulis, S.L., MacLean, P.J., Davidson, R., and Weisener, C.G., 1993, Arsenian pyrite from gold deposits, Au and As distribution invested by SIMS and EMP, and color staining and surface oxidation by LIMS: Canadian Mineralogist, v. 31, p. 1–17.

Geological Survey of Iran, 1995, Explanatory text of geochemical map of Moaleman (6960), Report 9, v. 1, 33 p.

Giggenbach, W.F., and Stewart, M.K., 1982, Processes controlling the isotopic composition of steam and water discharges from steam vents and steam-heated pools in geothermal areas: Geothermics, v. 11, p. 71–80.

Goldstein, R.H., and Reynolds, T.J., 1994, Systematics of fluid inclusions in diagenetic minerals: Society of Economic Paleontologists and Mineralogists Short Course 31, 199 p.

Haas, J.L., Jr., 1971, The effect of salinity on the maximum thermal gradient of a hydrothermal system at hydrostatic pressure: Economic Geology, v. 66, p. 940–946.

Hassanzadeh, J., Ghazi, A.M., Axen, G., and Guest, B., Stockli, D., and Tucker, P., 2002, Oligocene mafic-alkaline magmatism in north and northwest of Iran: Evidence for the separation of the Alborz from the Urumieh-Dokhtar magmatic arc [abs.]: Geological Society of America Abstracts with Program, v. 34, no. 6, p. 331.

Hedenquist, J.W., and Henley, R.W., 1985, Effect of CO_2 on freezing point depression measurements of fluid inclusions: Evidence from active systems and application to epithermal studies: Economic Geology, v. 80, p. 1379–1406.

Hedenquist, J.W., Reyes, A.G., Simmons, S.F., and Taguchi, S., 1992, The thermal and geochemical structure of geothermal and epithermal systems: A framework for interpreting fluid inclusion data: European Journal of Mineralogy, v. 4, p. 989–1015.

Hedenquist, J.W., Arribas R., A., and Gonzalez-Urien, E., 2000, Exploration for epithermal gold deposits: Reviews in Economic Geology, v. 13, p. 245–277.

Henley, R.W., 1985, The geothermal framework of epithermal deposits: Reviews in Economic Geology, v. 2, p. 1–24.

Hushmandzadeh, A.R., Alavi Naini, M., and Haghipour, A.A., 1978, Evolution of geological phenomenon in Totud area: Geological Survey of Iran Report H5, 136 p. (in Farsi).

John, D. A., 2001, Miocene and early Pliocene epithermal gold-silver deposits in the northern Great Basin, western United States: Characteristics, distribution, and relationship to magmatism: Economic Geology, v. 96, p. 1827–1853.

Khalatbari, M., 2000, Geological map of Abbas Abad: Geological Survey of Iran.

Kousari, S., 2001, Detail geochemical exploration in Gandy ore field, Moaleman area, southern Damghan: Geological Survey of Iran, unpublished report, 210 p.

McDonough, W.F., and Sun, S.-S., 1995, The composition of the earth: Chemical Geology, v. 120, p. 223–253.

Ohmoto, H., and Goldhaber, M.B., 1997, Sulfur and carbon isotopes, *in* Barnes, H.L., ed., Geochemistry of hydrothermal ore deposits, 3rd ed.: New York, John Wiley and Sons, p. 517–611.

Pearce, J.A., and Peate, D.W., 1995, Tectonic implications of the composition of volcanic arc magmas: Annual Review of Earth and Planetary Science, v. 23, p. 251–285.

Roedder, E., 1984, Fluid inclusions: Reviews in Mineralogy, v. 12, 644 p.

Seward, T.M., and Barnes, H.L., 1997, Metal transport by hydrothermal ore fluids, *in* Barnes, H.L., ed., Geochemistry of hydrothermal ore deposits, 3rd ed.: New York, John Wiley and Sons, p. 435–486.

Shamanian, G.H., 1998, Hammer prospecting of gold in Arghash area (scale 1:20,000), southern Nishabour, Khorasan province, Iran: Geological Survey of Iran, unpublished report, 100 p. (in Farsi).

Simon, G., Huang, H., Penner-Hahn, J.E., Kesler, S.E., and Kao, L.S., 1999, Oxidation state of gold and arsenic in gold-bearing arsenian pyrite: American Mineralogist, v. 84, p. 1071–1079.

Simmons, S.F., 1991, Hydrothermal implications of alteration and fluid inclusion studies in the Fresnillo district, Mexico: Evidence for a brine reservoir and a descending water table during the formation of hydrothermal Ag-Pb-Zn orebodies: ECONOMIC GEOLOGY, v. 86, p. 1579–1601.

Simmons, S.F., Gemmell, B., and Sawkins, F.J., 1988, The Santo Nino silver-lead-zinc vein, Fresnillo district, Zacatecas, Mexico: Part II. Physical and chemical nature of ore-forming solutions: ECONOMIC GEOLOGY, v. 83, p. 1619–1641.

Spies, O., Lensch, G., and Mihm, A., 1983, Geochemistry of the post-ophiolitic Tertiary volcanics between Sabzavar and Quchan/NE-Iran: Geological Survey of Iran Report 51, p. 247–267.

Taheri, J., and Shamanian, G.H., 2001, Geological map of Kashmar (scale 1:100,000): Geological Survey of Iran.

Webster, J.G., and Mann, A.W., 1984, The influence of climate, geomorphology and primary geology on the supergene migration of gold and silver: Journal of Geochemical Exploration, v. 22, p. 21–42.

Appendix 1

Description of Rock Samples

Abbreviations: Bt = biotite, Cal = calcite, Fs = feldspar, Hbl = hornblende, Pl = plagioclase, Qtz = quartz

Sample no. Ga-M-41, Calcareous sandstone
Description: This sample consists of angular clasts of Qtz (0.1–0.2 mm, 15 vol %), Pl (0.1–0.2 mm, 10 vol %), alkali Fs (0.1–0.2 mm, 5 vol %) that is partially altered to clay minerals and opaque minerals. The matrix is composed of Cal and very fine grained Qtz. Remarks: This rock is poorly sorted and immature in texture and mineralogy (i.e., for alkali Fs).

Sample no. Ga-M-31, Felsic tuff
Description: Anhedral Qtz (0.05–2 mm, 10 vol %) and opaque oxides (0.02–0.05 mm, <5 vol %) disseminated in a crypto- to microcrystalline groundmass.

Sample no. 79/H78, Felsic tuff
Description: Anhedral Qtz (0.05–2 mm, 10 vol %) and opaque oxides (0.02–0.05 mm, <5 vol %) disseminated in a crypto- to microcrystalline groundmass.

Sample no. Ga-M-8, Andesitic lava
Description: The phenocrysts consist of Hbl (1 mm, 0.5 vol %) and Pl (0.7–1 mm, 10 vol %). The groundmass consists of microlites of euhedral to subhedral Pl (0.1–0.3 mm).

Sample no. Ga-M-10, Andesitic lava
Description: The phenocrysts consist of weakly zoned Pl (1–3.5 mm, 15 vol %) and Hbl, which is rimmed by opaque iron oxides. This rim is caused by dehydration and oxidation of Hbl upon extrusion (1–2 mm, 5 vol %), Cal is pseudomorphous after Pl (0.5–1 mm, 5 vol %). The groundmass (grains avg 0.05 mm diam) consists mainly of Pl and opaque minerals (Fe-Ti oxides).

Sample no. 79/H40, Andesitic lava
Description: The phenocrysts consist of Hbl (1–2 mm, 5 vol %) and Pl (0.7–4 mm, 10 vol %). The groundmass consists of microlites of euhedral to subhedral Pl (0.1–0.2 mm).

Sample no. TR-52-7, Andesitic lava
Description: The phenocrysts consist of Hbl (1–2 mm, 5 vol %) and Pl (1–3 mm, 10 vol %). The groundmass consists of microlites of Pl (0.5–0.7 mm).

Sample no. Zr-41, Sandstone
Description: This sample consists of clasts of Qtz (0.1–0.2 mm, 25 vol %) and Pl (0.1 mm, 2 vol %) cemented by fine to microcrystalline Qtz.

Sample no. Ga-M-14, Rhyolitic dome
Description: The phenocrysts consist of Qtz (0.3–1.5 mm, 10 vol %) and sanidine (0.3–1 mm, 5 vol %). The groundmass is microcrystalline.

Sample no. 79/H12, Rhyolitic dome
Description: The phenocrysts consist of Qtz (0.5–1.2 mm, 10 vol. %) and sanidine. The groundmass consists of the same minerals. Weak flow banding is present.

Sample no. Zr-22, Andesitic lava
Description: The sample contains mainly of microlites of Pl (0.1–0.6 mm, 35 vol %), augite (0.3–1 mm, 10 vol %), with minor opaque oxides.

Sample no. 79/A3, Andesitic lava
Description: The phenocrysts consist of Pl (0.3–1.5 mm, 25 vol %), hornblende (0.4–2 mm, 10–15 vol %), which is rimmed by opaque iron oxides, augite (0.3 mm, <5 vol %), and minor opaque minerals.

Sample no. TA1/6, Andesitic lava
Description: The sample consists of Pl (0.5–1.5 mm, 20 vol%) and augite (0.5–1 mm, 5 vol %), with minor opaque oxides. The groundmass consists of microlites of Pl.

Sample no. 79/A37, Andesitic lava
Description: The phenocrysts consist of Pl (1–2 mm, 15 vol %), Hbl (0.3–1mm, 5 vol %), and augite (<1 mm, <5 vol %). The groundmass consists of microlites of Pl.

Sample no. Zr-4, Rhyodacitic dike
Description: The phenocrysts consist of Qtz (0.5–1.5 mm, 10 vol %), Pl (0.4–3 mm, 15 vol %), sanidine (0.3–1mm, 5 vol %), and opaque minerals. The groundmass consists of the same minerals.

Sample no. Zr-5, Monzodioritic dike
Description: Phenocrysts consist of Pl (1–2 mm, 15 vol %), augite (0.3–1 mm, 5 vol %), and Hbl (0.3–0.8 mm, <5 vol %). The phenocrysts are surrounded by small Pl and Hbl.

Sample no. 79/A16, Quartz monzonite
Description: This hollocrystalline rock consists of subhedral Pl (1–3mm, 15 vol %), alkali Fs (<1 mm, 5 vol %), Qtz (<1mm, 5 vol %), Bt (0.5–1 mm, <5 vol %), and Hbl (0.5–1.5 mm, <5 vol %).

Sample no. 79/A13, Granite
Description: This rock consists of coarse-grained Qtz (0.5–2.5 mm, 15 vol %), alkali Fs (3–4 mm, 15 vol %), Pl (2–4 mm, 5 vol %), and Bt (1–2 mm, <5 vol %).

APPENDIX 2a

Composition of Gold

Sample no.	79/H59	GN-1	80/HG2	79/H63	GA1	TR1	GN-2
No. of analyses	3	4	1	2	3	1	1
			Wt %				
Au	87.7–89.5	87.5–90.9	90.8	88.0–89.1	85.1–89.4	87.7	90
Ag	11.6–13.5	11.0–12.9	7.2	10.9–13.1	11.0–14.6	13	11.7
Cu	1.4–1.6	<0.01–0.7	0.1	0.1–0.04	0.04–0.07	0.12	0.08
Hg	<0.01–0.17	<0.01–0.03	<0.01	0.06–0.1	<0.01–0.03	0.02	<0.01
Total	102.8	100.03	98.1	102.4	99.8	100.1	101.81
			Atom %				
Au	75.1–77.8	77.8–81.9	87.1	78.6–81.5	75.9–81.5	78.4	80.7
Ag	18.4–21.1	18.1–20.9	12.6	18.3–21.1	18.3–23.8	21.2	19.1
Cu	3.66–4.13	0.0–1.88	0.30	0.11–0.27	0.11–0.19	0.33	0.19
Hg	0.0–0.14	0	0	0.001–0.11	0	0	0
Enclosing mineral	Cc, Gn	Gn, Ccp	Goe		Partially oxidized Py	Partially oxidized Py	Fe-(hydr)oxide

Abbreviations: Cc = chalcocite, Ccp = chalcopyrite, Goe = goethite, Gn = galena, Py = pyrite

APPENDIX 2b

Composition of Sphalerite

Sample no.	79/H59	80/HG20	79/H90	GAM3	GN1	GN2	Tch/6	Tch/12	Tch/19	TA1/2	TA1/14
No. of analyses	5	2	1	2	1	2	3	2	2	2	3
						Wt %					
Zn	64.8–66.19	65.37–65.65	65.29	66.49–67.47	65.71	66.01–66.74	66.20–67.1	65.80–66.5	67–67.1	65.8–66.8	66.9–67.4
Fe	0.51–0.77	0.57–0.67	1.02	0.44–0.87	0.90	0.68–0.80	0.1–0.90	0.8–1.70	0.20	0.7–0.8	0.6–1.0
Cd	0.33–0.42	0.41–0.45	0.35	0.36–0.63	0.21	0.55–0.63	0.20–0.3	0.30	0.1–0.2	0.1–0.2	0.2–0.3
S	32.0–32.76	31.91–31.79	32.71	32.1–32.92	32.26	32.41–32.80	31.3–32.3	31.0–31.6	32.2–32.5	32.4–32.5	32.1–32.5
Total	100.13	98.26	99.37	100.03	99.08	100.46	98.80	99.20	99.80	99.20	100.00
						Mol %					
ZnS	98.3–98.8	98.63–98.43	97.90	98.01–98.93	98.24	98.13–98.29	98.26–99.57	96.82–98.36	99.48–99.57	98.51–98.61	98.03–98.72
FeS	0.87–1.34	1.01–1.18	1.79	0.76–1.50	1.58	1.17–1.39	0.17–1.56	1.39–2.93	0.35	1.21–1.40	1.03–1.71
CdS	0.35	0.31–0.36	0.31	0.31–0.53	0.18	0.48–0.54	0.17–0.26	0.26	0.09–0.17	0.09–0.17	0.17–0.26

APPENDIX 2c

Composition of Pyrite

Sample no.	GaM3	78H59	Zr10	Tch/6	TA1/14	TA1/10	Zr11
No. of analyses	14	4	1	1	2	2	2
				Wt %			
Fe	43.0–47.0	42.7–46.0	47.2	46.9	47.2–47.4	46.78–46.9	46.33–46.9
Co	<0.02–0.1	<0.02	0.04	<0.02	<0.02	<0.02	<0.02–0.02
Ni	<0.02–0.04	<0.02–0.07	0.03	<0.02	0.02–0.04	<0.02–0.02	<0.02
Cu	<0.02–0.04	0.1–1.7	<0.02	0.02	<0.02	<0.02	<0.02
As	<0.02–6.03	0.4–6.4	<0.02	<0.02	<0.02	0.2–1.9	<0.02
S	50.3–53.9	49.6–52.9	53.1	52.8	53.6–53.7	52.6–53.7	53.4–53.7
Total	99.94	98.87	100.37	99.72	101.12	101.3	99.76
				Formula (basis 1 atom per formula)			
Fe	0.32–0.33	0.32–0.33	0.34	0.34	0.34	0.33	0.33
As	0.0–0.015	0.002–0.015	0	0	0	0	0
Total M site	0.33	0.32–0.33	0.34	0.34	0.34	0.33	0.33
As	0.0–0.033	0.002–0.035	0.000	0.000	0.000	0.010	0.000
S	0.635–0.667	0.632–0.665	0.667	0.667	0.667	0.657–0.666	0.667
Total XY site	0.667	0.667	0.667	0.667	0.667	0.667	0.667

APPENDIX 3

Homogenization and Ice-Melting Temperatures of Fluid Inclusion Assemblages in Sphalerite from Gandy (sample locations shown in Fig. 4)

Sample no.	Type	$T_{m(ice)}$ range (°C) Low/mean/high (no. inclusions)	Salinity (mean) Wt % NaCl equiv	T_h range (°C) Low/mean/high	Comments
GA-M-3	S			195/216/225 (12)	In clear core
	P			231/237/243 (3)	In clear core
	PS			248/251/252 (14)	In yellow border
	P			236/242/245 (5)	In yellow border
	P			274 (1)	In yellow border
	P			284 (1)	In yellow border
	S			222/222/224 (13)	In clear core
	P			230/234/243 (14)	In clear core
	PS			240/241/241 (4)	In yellow border
	S			201/202/202 (6)	In clear, core
	S			224/225/226 (12)	In clear core
	P			257/258/258 (3)	In clear core
	P			259/261/262 (13)	In clear core
	P			234/235/239 (10)	In yellow border
	P			258/259/260 (10)	In clear core
	S			208 (6)	In clear core
	P			253 (2)	In yellow border
	P	–2.7 (1)	4.5	232/234/240 (9)	In yellow border
	P			290 (1)	In yellow border
	P			258 (1)	In clear core
	P			254 (1)	In yellow border
	PS			243 (2)	In yellow border
	S			180/186/198 (8)	In yellow border
	PS			239 (3)	In yellow border
	S			150/151/152 (9)	In yellow border
	P			244/245/248 (9)	In yellow border
	P			277 (1)	In yellow border
	PS			250/251/252 (8)	In clear core
	PS			250/252/254 (6)	In clear core
	PS			267 (2)	In clear core
	P			320 (1)	In clear zone, necked?
	PS			252/253/254 (11)	In clear core
	PS			254/255/255 (8)	In clear core
	PS			253 (2)	In clear core
	PS			253 (2)	In clear core
	P			356 (1)	In clear zone, necked
	PS			252/253/253 (3)	In clear core
	P			246/247/247 (7)	In yellow border
	S			208/206/220 (13)	In yellow border
	P	–2.9 (1)	4.8	253 (2)	In yellow border
	S			227 (5)	In yellow border
	P			241/242/244 (6)	In yellow border
	P	–2.6 (3)	4.3	244/246/247 (6)	In yellow border
	P			250/251/252 (2)	In clear core
	P			254 (2)	In yellow border
	P			254 (1)	In yellow border
	P			255 (1)	In clear core
	P			256 (2)	In clear core
	P			252 (1)	In yellow border
	P			248 (1)	In yellow border
	P			242 (1)	In yellow border
	P			265/266/266 (9)	In clear zone, necked
	P			238 (1)	In clear core
	P			244/245/246 (5)	In clear core
	P			250/251/252 (2)	In clear core
	PS	–2.7 (2)	4.5	251/253/257 (10)	In clear core
	PS			251/253/258 (3)	In clear core
	P			248 (3)	In clear core
	P			255 (2)	In yellow border
	PS			253 (4)	In yellow border
	PS			253/259/264 (7)	In yellow border
	PS			253/254/257 (8)	In yellow border
	PS	–3.3/–3.2/–3.2 (4)	5.3	258/260/263 (5)	In clear core
	PS			251/252/252 (6)	In yellow border
	S			222/225/230 (10)	In clear core
	P	–2.5 (2)	4.2	251/253/257 (3)	In clear core
	P	–2.9 (1)	4.8	253/254/255 (13)	In clear core
79/H51	PS			246 (3)	In clear core
	P	–2.5 (1)	4.2	243 (2)	In yellow border
	P	–3.1 (1)	5.1	256/256/257 (10)	In clear core
	P			244 (1)	In clear core
	P	–3.1 (3)	5.1	253/254/255 (12)	In clear core
	P			256/257/258 (6)	In clear core
	S			216 (6)	In clear core
	S			194 (5)	In clear core
	PS			243 (7)	In clear core
	P			308 (1)	in clear zone, necked?
	PS			247/252/254 (3)	In yellow border
	P	–3.0 (1)	5.0	257 (1)	In clear core
	P			242/242/243 (3)	In yellow border
79/H59	S			168 (5)	In clear core
	S			217 (6)	In clear core
	P	–3.1 (2)	5.1	262/263/264 (3)	In yellow border
	P	–3.2 (1)	5.3	267 (4)	In yellow border
	PS			259/259/260 (8)	In clear core
	PS			233/235/236 (4)	In yellow border
	PS			248/248/249 (8)	In yellow border
	P	–3.3 (2)	5.4	283/285/287 (2)	In clear core
	S			217 (6)	In clear core
	PS			273/273/274 (7)	In clear core
	PS			266 (7)	In clear core
	P			>350 (1)	In clear zone, necked

Notes: Number of measured inclusions in each fluid inclusion assemblage shown in parentheses; where T_m value is constant, only one value is listed; Abbreviations: P = primary, PS = pseudosecondary, S = secondary inclusions

APPENDIX 4

Homogenization and Ice-Melting Temperatures of Fluid Inclusion assemblages from Abolhassani (sample locations shown in Fig. 5)

Sample no.	Type	$T_{m(ice)}$ (°C) Low/mean/high	Salinity Wt % NaCl equiv	T_h range (°C) Low/mean/high	Comments
Tch-6	P	–12.6/–12.5/–12.4 (2)	16.4	331/336/337 (5)	
	P	–4.2 (1)	6.7	241/242/243 (2)	
	P			301/302/303 (10)	
	P			256 (1)	
	P			240/241/243 (6)	
	P	–14.5 (1)	18.2	336/340/345 (4)	
	P	–6.2 (1)	9.5	249/250/252 (9)	
	P			284/300/322 (3)	
	S			181/183/185 (8)	
	S			156/157/158 (7)	
	S			206/208/209 (9)	
	S			111/112/115 (11)	
	S			111/112/115 (16)	
	S			136/137/140 (11)	
	S			203 (3)	
	P			243/244/244 (6)	
	P			233/234/235 (9)	
	S			154 (7)	
	S			121 (3)	
	P			284 (2)	
	P	–6.6 (1)	10.0	269 (1)	
	PS	–4.2 (1)	6.7	243 (2)	
	P			290 (3)	
	P			275/286/321 (4)	
	S			111/115/120 (10)	Qtz
Tch-12	S			142/143/144 (8)	
	S			148/152/154 (11)	
	P			247/248/249 (5)	
	PS			236/236/237 (5)	
	PS			273 (3)	
	P			257/257/258 (6)	
	P	–14.9 (2)	18.5	286/301/327 (9)	
	PS	–15.6/–15.1/–14.1 (4)	18.7	282/338/354 (6)	
	S			233 (5)	
	P			291/292/298 (9)	
	S			126/127/128 (6)	
	P			296 (3)	
TA1-14	S			117/118/118 (10)	
	S			188/189/190 (4)	
	P	–10.2 (1)	14.1	288 (1)	Necked
	P			268 (3)	
	P			303/304/304 (5)	
	P			244 (1)	
	S			211/211/212 (7)	
	PS	–9.6 (2)	13.5	268/273/274 (7)	
	PS			266 (2)	
	P	–9.6 (1)	13.5	234/236/238 (2)	
	PS			273 (4)	
	PS			271/272/273 (5)	
	P			276/276/277 (8)	
	P			243 (2)	
	P			>350 (1)	Necked
	PS			243/244/244 (5)	
	P			294 (2)	
	S	–14.3 (2)	18.0	215/216/216 (9)	
	P			305/316/322 (3)	
	S			141 (5)	Qtz

Notes: Number of measured inclusions in each fluid inclusion assemblage shown in parentheses; all samples are sphalerite, except as noted
Abbreviations: P = primary inclusions, PS = pseudosecondary inclusions, Qtz = quartz, S = secondary inclusions